NASA TECHNICAL NOTE

NASA TN D-3086

SOLAR CYCLE EFFECTS ON INNER ZONE PROTONS

by R. C. Blanchard and W. N. Hess

Goddard Space Flight Center
Greenbelt, Md.

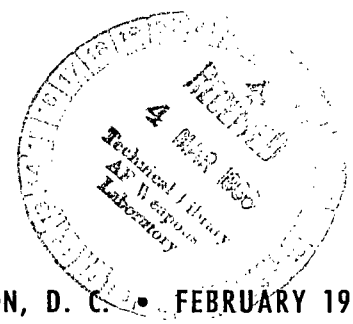

NATIONAL AERONAUTICS AND SPACE ADMINISTRATION • WASHINGTON, D. C. • FEBRUARY 1966

NASA TN D-5086

SOLAR CYCLE EFFECTS ON INNER ZONE PROTONS

By R. C. Blanchard
and W. N. Hess

Goddard Space Flight Center
Greenbelt, Md.

NATIONAL AERONAUTICS AND SPACE ADMINISTRATION

For sale by the Clearinghouse for Federal Scientific and Technical Information
Springfield, Virginia 22151 – Price $2.00

ABSTRACT

Solar cycle variations of the proton population of the inner radiation belt are calculated in this report. The analysis includes proton energies from 10 to 700 Mev, field lines from 1.2 to 1.6 earth radii, and appropriate values of field strength. An averaged atmospheric model is constructed in terms of B (flux density in gauss) and L (earth radii) coordinates which represents the average proton number density that trapped particles would encounter. The averaging process includes diurnal, longitudinal, north-south, and "bounce" averaging. The time dependence of the atmospheric model is constructed for the current cycle using averaged information of the 10.7-cm solar flux of the recent past. Proton flux spectra for solar minimum and solar maximum are calculated from the particle conservation equation. Transient proton spectra and time histories are presented showing the dynamical behavior of trapped protons when influenced by the fluctuating atmosphere and a variable source. The results indicate that in the region of B-L space corresponding to minimum altitudes of 300 to 800 km, the proton flux is changed appreciably from solar maximum to solar minimum where solar minimum is the larger. Calculations indicate a change in the nature of the proton spectra where the spectra become peaked at some energy level depending on the time in the cycle and position in space. Comparisons are made with available data.

CONTENTS

SOLAR CYCLE EFFECTS ON INNER ZONE PROTONS

by
R. C. Blanchard
and W. N. Hess
Goddard Space Flight Center

INTRODUCTION

The purpose of this paper is to calculate the expected changes in inner-zone proton densities with time in the solar cycle. Freden and White identified the penetrating component of the inner belt as due to energetic protons (Reference 1). Subsequent experimental work by Freden and White (References 2 and 3), and Armstrong, Harrison, Heckman, and Rosen (Reference 4) has extended this finding and we now have a well-established proton energy spectrum at earth radii, L, approximately equal to 1.4, and flux density, B, approximately equal to 0.20 for a time near solar maximum (Figure 1). Their measurements have established the energy spectrum of the protons for $E > 20$ Mev. The analysis of this spectrum (Reference 3) by an albedo neutron decay source mechanism suggests that this source adequately describes the production of protons of the inner zone.

One of the features of this component of the belt is its time consistency. Measurements after a solar flare by Freden and White (Reference 3) indicated little variation in proton flux. Yoshida, Ludwig, and Van Allen (Reference 5) have shown from Explorer I data that the change in the proton population is less than a factor of 2 for a two-month period. Data from Explorer IV (Reference 6) indicated the same results for a three-month period in 1958. Data from Explorer VII (Reference 7) collected for a 15-month period indicated a net change by a factor of about 4 or 5 at the outer part of the inner zone to about 2 or 3 at the inner part of the inner zone. Although the net change in Explorer VII data is not pronounced, it does show a steady increase in the counting rate with some superimposed variations. Hess (Reference 8) has shown that slow changes in proton population were expected due to solar-cycle effects on the galactic cosmic ray flux and, more importantly, on the fluctuating atmosphere due to solar exospheric heating. It turns out that these two factors are resonant, producing a larger proton flux at solar minimum than at solar maximum. Hess (Reference 9) estimated this factor to be 10 or more over a solar cycle. It is believed that some of the steady increase in the counting rate from Explorer VII at a time approaching solar minimum could be due to the solar-cycle effect. This report will examine the solar-cycle effect on inner-zone protons to determine its characteristics in detail.

CONTINUITY EQUATION

The study of the variation in the proton population requires knowledge of the conditions which govern the source and loss of protons in a given region. The continuity equation for inner-zone protons is usually written as (References 2, 10 and 11)

$$\frac{dN(E)}{dt} = S(E) - L(E) + \frac{d}{dE}\left(Nv\frac{dE}{dv}\right), \qquad (1)$$

where S(E) is the albedo neutron decay source of protons being supplied to the region; L(E) is the nuclear interaction loss of protons in the region; and the last term includes the effect of proton energy loss due to near coulomb collisions with bound atmospheric atoms. This equation approximately represents the conservation condition of trapped protons, which yields the rate of change of the proton number density, while integration of this equation gives the total proton number density at a given energy level, E, in protons/cm^3-Mev.

The loss term L used in this study is basically that used by Freden and White (Reference 2) with some modifications. The term takes into account catastrophic nuclear collisions of trapped protons with the atmospheric atoms. This term is written as

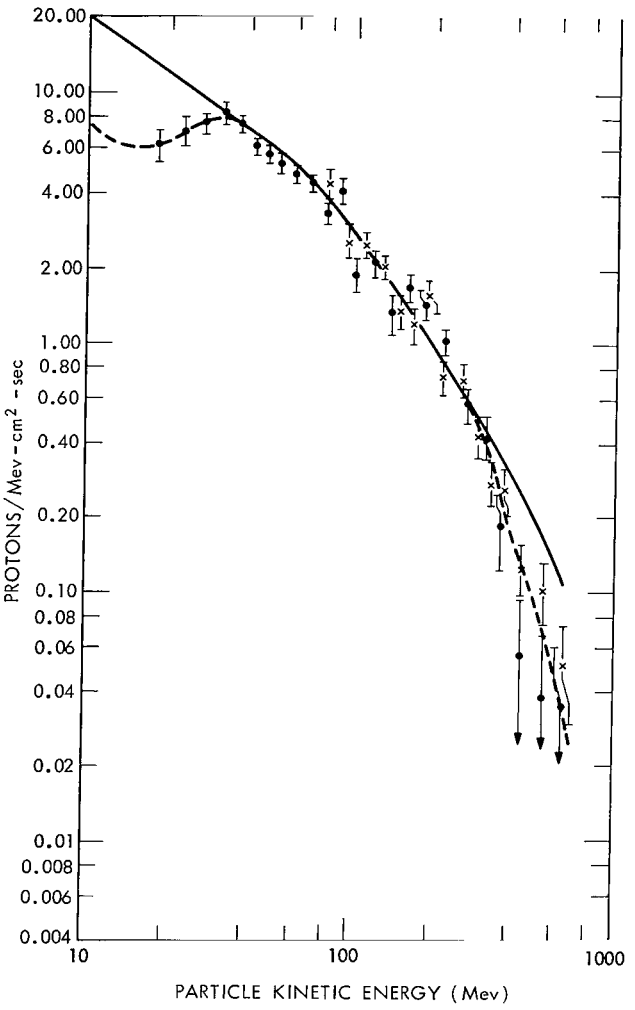

Figure 1—The experimentally measured inner-zone proton energy spectrum (Freden and White, Reference 3) for L ~ 1.4, B ~ 0.20 at time near solar maximum.

$$L = Nv\sum_{j=1}^{5}\bar{\bar{n}}^j\sigma(j), \qquad (2)$$

where j refers to the atmospheric components considered, which are O_2, O, N_2, He, and H, $\bar{\bar{n}}^j$ is the average atmospheric density of the j^{th} constituent and $\sigma(j)$ is the inelastic geometric cross section of the j^{th} constituent. By defining

$$\Sigma = \sum_{j=2}^{5}\bar{\bar{n}}^j\sigma(j), \qquad (3)$$

Equation 2 can be written more conveniently as

$$L = Nv\Sigma \quad . \tag{4}$$

The values of σ for oxygen and helium used in this study are

$$\sigma(O) = 0.36 \text{ barns}$$

and

$$\sigma(He) = 0.143 \text{ barns} \quad .$$

For simplicity of calculation, it is assumed that the nitrogen interaction cross section is equal to that of oxygen and the hydrogen contribution is negligible. Thus, the calculation of Σ is made by the relation:

$$\Sigma = \frac{\bar{\bar{n}}^{(He)}}{2}\sigma(He) + \left[\frac{\bar{\bar{n}}^{(O)}}{8} + \frac{2\bar{\bar{n}}^{(O_2)}}{} + \frac{2\bar{\bar{n}}^{(N_2)}}{7}\right]\sigma(O). \tag{5}$$

The pulsation of the atmosphere causes Σ to be a function of time in the solar cycle as well as position. Figure 2 shows a time history of $\log_e \Sigma$ for various values of B at L = 1.25. It can be seen that as B increases, the variation from solar maximum to solar minimum decreases. The fluctuating atmosphere is not as pronounced at large flux densities which correspond to low altitudes.

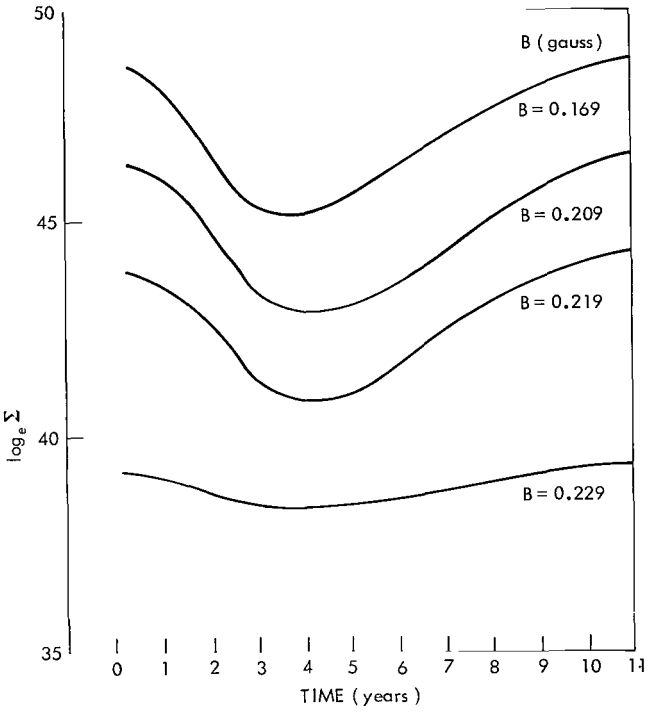

Figure 2—A time history of the "effective" cross section of the atmosphere, Σ as a function of B at L = 1.25 e.r.

The source term S(E) used in this study is from albedo neutron decays. The neutrons are produced from cosmic ray protons colliding with atmospheric oxygen and nitrogen. The produced neutrons diffuse out from the atmosphere and subsequently decay into protons after approximately 10^3 seconds. The neutrons which escape from the atmosphere and then decay will be injected into the belt. The form of the proton source to be used is essentially the

same as that used by Hess (Reference 11) with some minor modifications. Specifically, these are the addition of the solar cycle time dependence and the transformation into B-L space. This leaves the source as:

$$S = \frac{0.8E^{-2}\Phi}{\beta C \gamma \tau L^2 \cos^4 \lambda} , \tag{6}$$

where

v = neutron velocity (cm/sec),

$\beta = v/c$,

C = speed of flight, 2.9979×10^{10} cm/sec,

$\gamma = (1-\beta^2)^{-1/2}$,

τ = neutron mean life, 10^3 sec, and

$0.8E^{-2}$ = calculated neutron flux (neutrons/cm^2-Mev-sec),

and where the magnetic latitude dependence, λ, is replaced by B through the dipole magnetic field equation. This $\cos^{-4}\lambda$ term is left in the equation due to the inability of the field equation to be solved readily in closed form. The nondimensional parameter Φ is the relative inner belt source strength. That is,

$$\Phi = \frac{\phi(t, E)}{\phi(t_0, E)} , \tag{7}$$

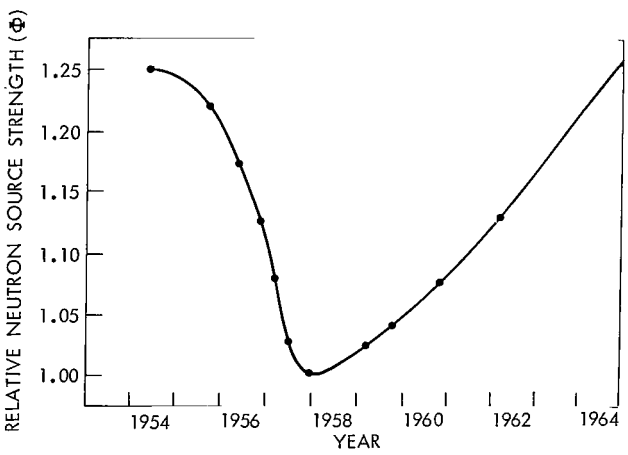

Figure 3—A time history of the relative inner-belt source strength.

where the nomalizing factor $\phi(t_0 E) = 0.8E^{-2}$ neutrons/cm^2-Mev-sec. The relative inner-belt source strength is a function of time in the solar cycle. Figure 3 is a plot of a current estimate* (Reference 12) of the change of Φ for the current solar cycle. Three points of interest in this graph are: first, the net change over the cycle is 25%; second, at solar maximum the production of neutrons is smallest due to exclusion of some neutron-producing galactic particles by the sun's increased activity; and third, Φ is not symmetrical.

It is assumed that the source, S, produces protons such that all produced protons have

*McDonald, F. B., private communication.

velocity orientations perpendicular to the field at the magnetic mirror latitude, λ. This assumption is made instead of adding the contributions of protons at other positions along a field line which have the necessary mirror point conditions (that is, the proper pitch angle). The assumption of an injection coefficient of 1 will probably not affect the overall result of the study, which is the relative change from solar minimum to solar maximum.

Equations 6 and 4 represent the form of the components of Equation 1. Approximate values of β and γ were generated by Freden and White (Reference 2). They are:

$$\left.\begin{aligned} \beta &= 0.0484E^{-.477} \\ \gamma &= 0.930E^{-.032} \end{aligned}\right\} \quad \text{for } 10 \leq E < 80 \text{ Mev}$$

$$\left.\begin{aligned} \beta &= 0.0896E^{-.344} \\ \gamma &= 0.428E^{-.205} \end{aligned}\right\} \quad \text{for } 80 \leq E < 700 \text{ Mev} \quad .$$

Utilizing these approximations and Equations 4 and 6, Equation 1 can be arranged in the following form:

$$\frac{dN}{dt} = \frac{a_0 \Phi}{L^2 E^{b_0} \cos^4 \lambda_m} - \frac{a_1 N}{E^{b_1}} \left(\frac{dE}{dX}\right) - a_2 N E^{b_2} \frac{d}{dE} \left(\frac{dE}{dX}\right) - a_2 E^{b_2} N\Sigma \qquad (8)$$

where, if the energy is $10 \leq E < 80$ Mev

$$a_0 = 2.694 \times 10^{-13} \qquad b_0 = 2.509$$

$$a_1 = 3.463 \times 10^{8} \qquad b_1 = 0.523$$

$$a_2 = 7.255 \times 10^{8} \qquad b_2 = 0.477$$

and if the energy is $80 \leq E < 700$ Mev

$$a_0 = 3.479 \times 10^{-13} \qquad b_0 = 2.549$$

$$a_1 = 4.617 \times 10^{8} \qquad b_1 = 0.656$$

$$a_2 = 1.343 \times 10^{9} \qquad b_2 = 0.344 \quad .$$

The calculation of the energy loss due to slowing down is approximately evaluated by

$$\frac{dE}{dX} = R \left(\frac{dE}{dX}\right)_{NTP} \quad , \qquad (9)$$

where the scale factor, R, is the ratio of the equivalent oxygen number density of the atmosphere to the oxygen number density at NTP conditions. That is,

$$R = \frac{1.75\bar{\bar{n}}^{(N_2)} + \bar{\bar{n}}^{(O)} + 0.25\bar{\bar{n}}^{(He)} + 2\bar{\bar{n}}^{(O_2)} + 0.125\bar{\bar{n}}^{(H)}}{2.69 \times 10^{19}} .$$

Figure 4 is a time history of R at L = 1.25 for various B's. Again the solar-cycle variation becomes apparent. The values of $(dE/dX)_{NTP}$ comes from experimental data published by Aron, Hoffman, and Williams (Reference 13) for protons penetrating an oxygen absorber. Figure 5 is the energy spectrum of this data for the energies of interest. In a similar fashion the energy slope of the energy loss is

$$\frac{d}{dE}\left(\frac{dE}{dX}\right) = R\left[\frac{d}{dE}\left(\frac{dE}{dX}\right)\right]_{NTP} , \qquad (10)$$

where the slope of dE/dX has been calculated from Figure 5 and represented in Figure 6. Using Equations 9 and 11, Equation 8 can be

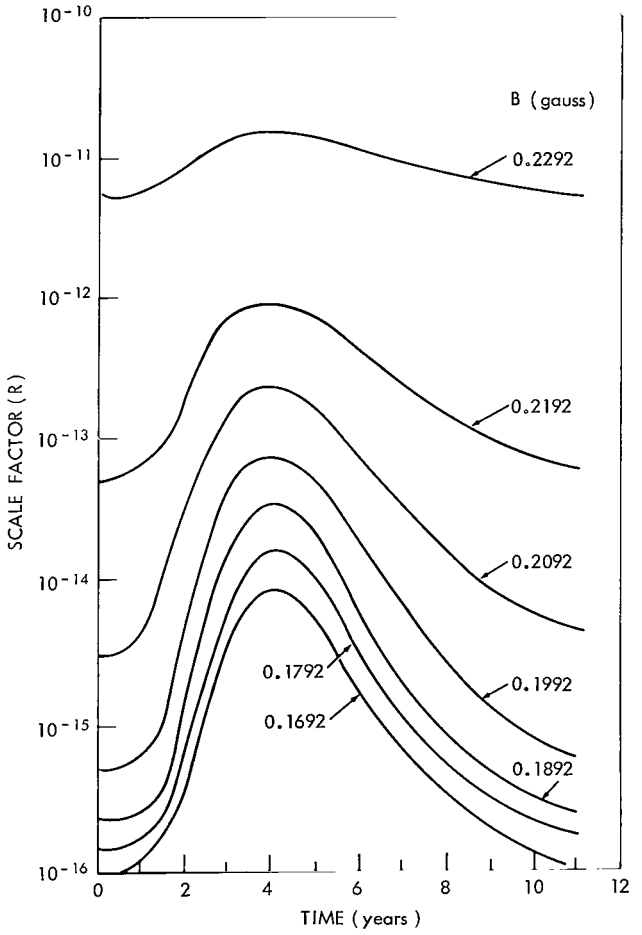

Figure 4—A time history of the atmosphere scale factor, R, as a function of B at L = 1.25 e.r.

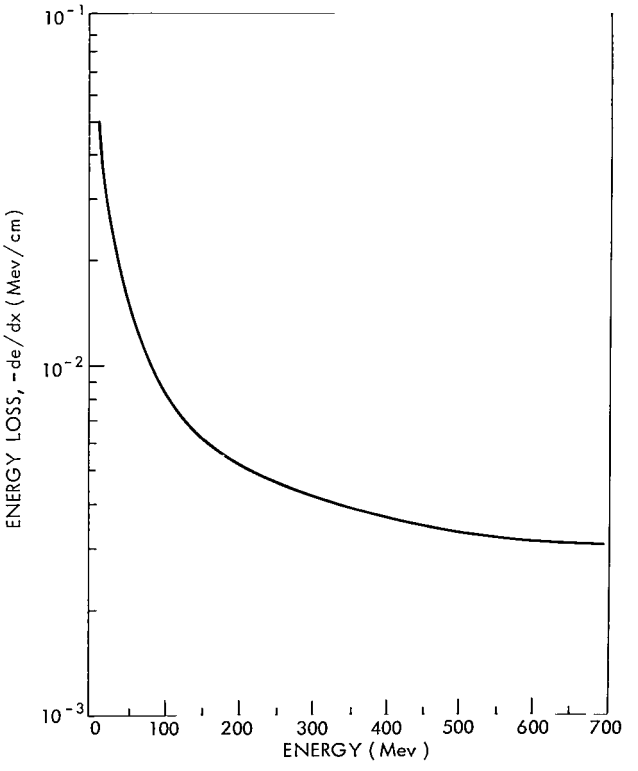

Figure 5—The proton energy loss spectrum for an oxygen target.

written as

$$\frac{dN}{dt} = \frac{a_0 \Phi}{L^2 E^{b_0} \cos^4 \lambda_m} - \frac{a_1 NR}{E^{b_1}} \left(\frac{dE}{dX}\right)_{NTP}$$

$$- a_2 N E^{b_2} R \left[\frac{d}{dE}\left(\frac{dE}{dX}\right)\right]_{NTP} - a_2 E^{b_2} N\Sigma \quad , \quad (11)$$

where the constants are those defined previously. A Fortran program has been written to numerically integrate Equation 11 where the functional dependence of the proton density rate is f(N, E, L, B, t).

A difficulty arises when evaluating the transient proton number density. As is evident from Equation 11, an initial value of N is necessary in order to integrate the equation. At time t_0 there are no trapped protons and the problem is started at solar minimum. This is done in order to investigate the most rapid build-up, since at solar minimum the injection of protons is the largest while the removal process is the smallest.

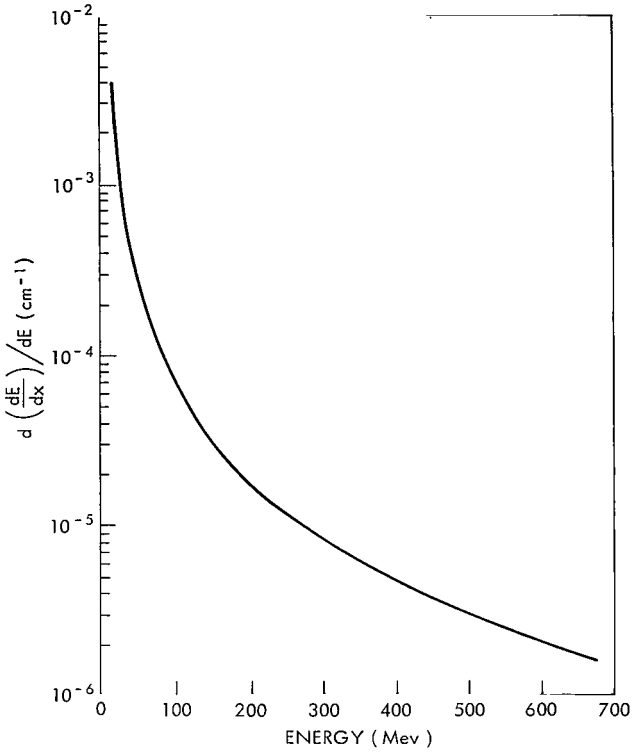

Figure 6—The slope of proton energy loss versus energy for an oxygen target.

Following the work done earlier (References 2, 10 and 11), the steady-state proton population is found by assuming the rate of change of the proton number density to be zero. The resulting solution of Equation 11 becomes:

$$N = \frac{a_0 \Phi}{L^2 E^{b_0} \left\{ \frac{a_1 R}{E^{b_1}} \left(\frac{dE}{dX}\right)_{NTP} + a_2 E^{b_2} \left[\frac{d}{dE}\left(\frac{dE}{dX}\right)\right]_{NTP} + a_2 E^{b_2} \Sigma \right\} \cos^4 \lambda_m} \quad , \quad (12)$$

where the coefficients are those defined previously. As can be seen from the functional dependence of N, a time must be chosen in order to evaluate the steady-state spectrum for a given position. Two times are chosen: maximum solar and solar minimum. This is done in order to investigate the maximum change in proton number density at the two source and loss extremes.

AVERAGE ATMOSPHERE IN B-L SPACE

A major part of this problem was to determine the average atmospheric density used in calculating the scale factor, R, which is contained in the loss-rate terms of trapped protons, and Σ, which

is contained in the nuclear interaction loss term. The calculation of these quantities has been done such that over a long sampling period, on the order of months, the values obtained would be representative of what a trapped particle would "see" while moving about the earth's magnetic field. Since the particle's three basic motions (that is, gyration around the field line, cyclic motion parallel to the field line and drift motion in longitude) are separated by large time differences (Reference 14), it is possible to consider them separately in the averaging process.

The model of the upper atmosphere used in the study is the one developed by Harris and Priester (Reference 15). This model gives the time dependences of the atmosphere for both solar cycle and diurnal variations. The atomic densities, n_i, of five atmospheric constituents (i.e., O_2, O, He, N_2, H) are given in the form

$$n_i = n_i (h, t, S) \quad ,$$

where h is the altitude above the earth, t is local time given in hourly increments and S is a model parameter related to, but not the same as the intensity of the 10.7 cm solar flux F in watts/$\left(m^2 - cps \times 10^{-22}\right)$. Harris and Priester's atmospheric model agrees well with several measurements of density by satellite drag (References 16 and 17) and has been checked by preliminary density data from the Explorer XVII satellite (References 18, 19 and 20). To date, this model is the most complete description of time dependence of atmospheric densities available and agrees well with current experimental data.

The first step in arriving at the average models is to calculate the diurnal average number density of each of the five S models presented by Harris and Priester. The sum,

$$\bar{n}^j (S) = \frac{1}{24} \sum_{i=1}^{24} n_i^j (S) \quad , \tag{13}$$

is computed, where the five atmospheric elements are j = He, O, O_2, N_2, H and where i refers to the hourly value of the density. The diurnal average is taken, since protons considered in this study drifting in longitude around the earth have periods of revolution on the order of 1 to 30 minutes (Reference 14). Thus, over a period of 24 hours, the daily proton population variation will tend to be averaged out, or at least to be a second-order effect compared to the solar-cycle expansion of the atmosphere which has a period of approximately 11 years. In essence, this step eliminates short-term time effects.

The second step in constructing the solar-cycle average atmosphere is to consider the longitudinal drift of protons along a B-L contour. As the particles drift around the earth, their mirror points encounter different altitudes, and, consequently, different atmospheric densities. To account for this, the calculation of the longitudinal average density, $\bar{\bar{n}}_k^j$, is done by the sum

$$\bar{\bar{n}}_k^j = \frac{1}{35} \sum_{i=1}^{36} \bar{n}_i^j (\phi) \quad , \tag{14}$$

where K refers to either Northern or Southern Hemisphere and where $\bar{n}_i^j(\phi)$ is the diurnal average number density of the j^{th} constituent at longitude ϕ. The factor 1/35 is used since equal increments of 10° in longitude were used to evaluate the summation. To obtain values of $\bar{n}^j$ as a function of longitude in each hemisphere, B-L contours (Reference 6) were generated (Reference 22) as a function of altitude and longitude. Figures 7 and 8 show these contours for a typical line of force, L = 1.25. Values of atmospheric number density as a function of longitude for each 10° were obtained by interpolating the results of Equation 13 for altitude which from Figures 7 and 8 corresponds to a given longitude for a given B and L. Upon evaluating Equation 14, the resulting functional dependence of the longitudinal-averaged atmosphere is

$$\bar{\bar{n}}_K^j = \bar{\bar{n}}_K^j (B, L, S)$$

Both hemispheres are then averaged. As can be seen from Figures 7 and 8, the Southern Hemisphere greatly influences the resultant atmosphere since it dips lowest in altitude due to the nature of the earth's magnetic field. Figure 9 is a plot of minimum altitudes for a B-L contour in the Southern Hemisphere. Plotting minimum altitude contours in B-L space indicates the region in

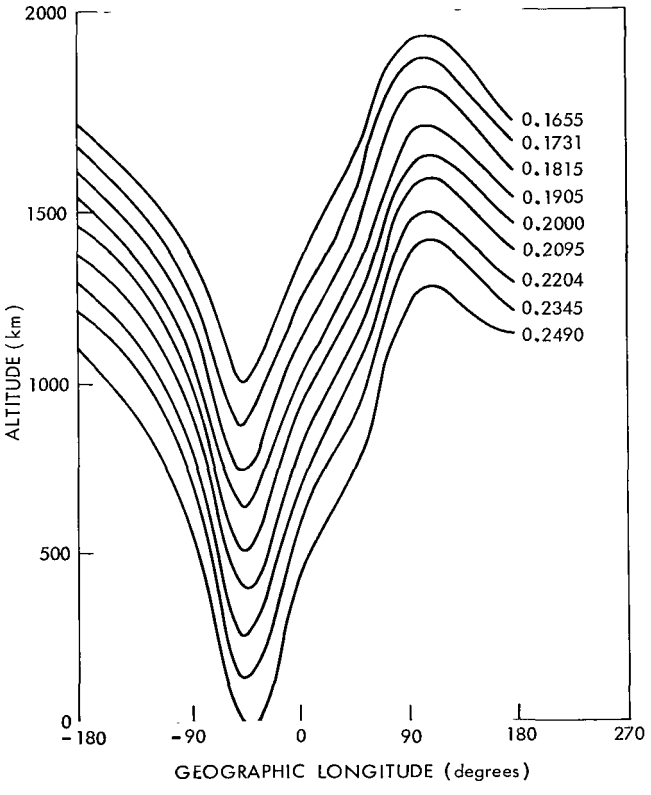

Figure 7—B (gauss) contours for L = 1.25 for the Southern Hemisphere as a function of altitude and geographic longitude.

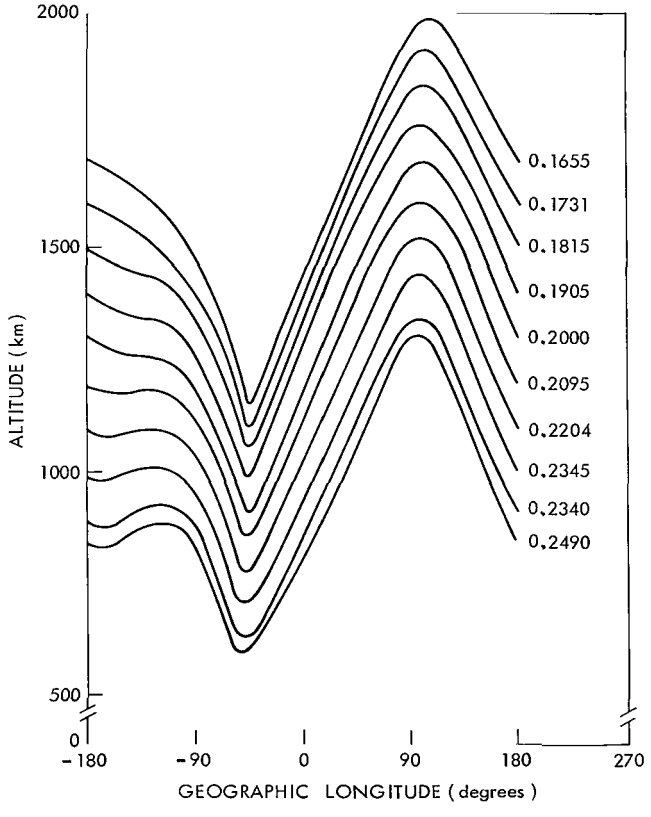

Figure 8—B (gauss) contours at L = 1.25 e.r. for the Northern Hemisphere of altitude and geographic longitude.

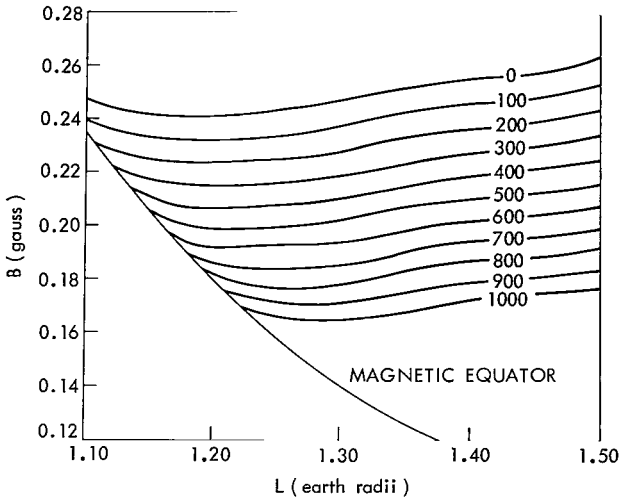

Figure 9—Minimum altitude contours in B, L space for the Southern Hemisphere.

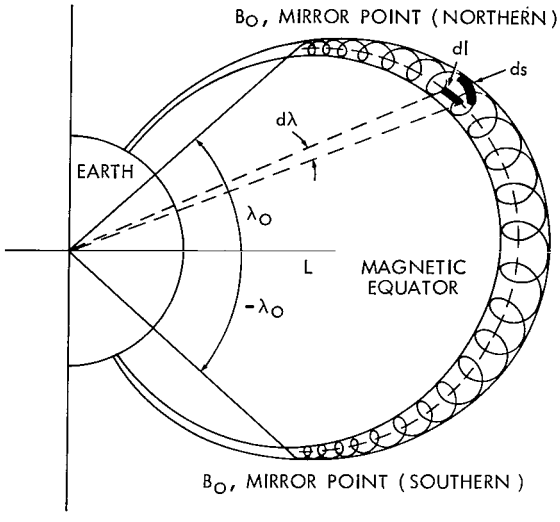

Figure 10—Schematic of a trapped particle's north-south motion where ds is the element of arc along the particle's helical trajectory, dl is the element of arc along the field line.

terms of B and L in which the atmosphere is appreciable as far as trapped particles are concerned. The assumption is made that protons drift with uniform velocity in longitude. This eliminates weighing the average process over longitude. Recently, Walt* indicated this is not the case. Thus, some error is introduced by not appropriately weighing the longitudinal averaging; probably about 20%.

The last averaging step is to adjust the longitudinal average density $\bar{\bar{n}}^j$ (B, L, S) due to the protons' north-south mirroring motion. This process reduces the magnitude of the tables due to motion of a proton from a mirror point at low altitude and high density moving towards the equator at a high altitude and low density. Since the protons live much longer than a bounce period, and since no change in direction of the proton is considered during slowing, it is permissible to average the density in this fashion. As one might expect, the account by which $\bar{\bar{n}}^j$ is reduced depends upon the arc distance away from the equator; as the arc distances approaches zero, the correction becomes unity. Following Ray (Reference 23), the bounce average of the number density is defined as

$$\bar{\bar{n}}^j = \frac{\int \bar{\bar{n}}(B, L, S)\, ds}{\int ds}, \qquad (15)$$

where ds is an element of arc along the particle's orbit. Figure 10 is a schematic of a trapped particle's north-south motion. The earth is assumed to be a dipole for the calculation of this averaging step. Due to symmetry, the integral need only be evaluated over a quarter of a complete oscillation. The procedure adapted for the calculation of Equation 15 is to project the element of arc onto the field line. This is done for convenience since the atmosphere is given in terms of field lines, L. The element of length along the particle's orbit is related to an element

*Walt, M., private communication.

of length along a field line by

$$ds = \frac{vdt}{\cos\alpha} = \frac{dl}{\cos\alpha} \quad ,$$

where α is the pitch angle (i.e., the angle between the velocity $\bar{v}$ and the magnetic field $\bar{B}$). By combining

$$dl^2 = dr^2 + r^2 d\lambda^2$$

along with the field equations

$$B = \frac{M}{r^3}\left(1 + 3\sin^2\lambda\right)^{1/2} \quad ,$$

$$r = L\cos^2\lambda \quad ,$$

and a relationship of the conservation of the magnetic moment, which is

$$\frac{\sin^2\alpha}{B} = \text{constant} \quad ,$$

reduces Equation 16 to

$$\bar{\bar{n}}^j = \frac{\int_0^{\lambda_m} \bar{\bar{n}}^j(\lambda)\, A(\lambda)\, d\lambda}{\int_0^{\lambda_m} A(\lambda)\, dl} \quad , \tag{16}$$

where

$$A(\lambda) = \cos^4\lambda\left[\frac{4 - 3\cos^2\lambda}{\sqrt{4 - 3\cos^2\lambda_m}\,\cos^6\lambda - \cos^6\lambda_m\sqrt{4 - 3\cos^2\lambda}}\right]^{1/2} . \tag{17}$$

The subscript m corresponds to the particle's mirror point. The weighing factor, $A(\lambda)$, appears in the averaging equations due to the fact that particles spiral about the field line in such a fashion as to stay longer at some latitudes, namely, near mirror latitudes, λ_m. Figure 11 is a plot of $A(\lambda)$ versus λ for different mirror latitudes, where the mirror latitudes (λ_m) are the asymptotes of each curve. A dipping of the curves occurs at $\lambda > 48°$ for large values of λ_m. This phenomena occurs principally because the lines of force become relatively steep for large mirror altitudes. For an equal $\Delta\lambda$, it turns out that the particle will spend less time at latitudes $> 48°$, and not near the

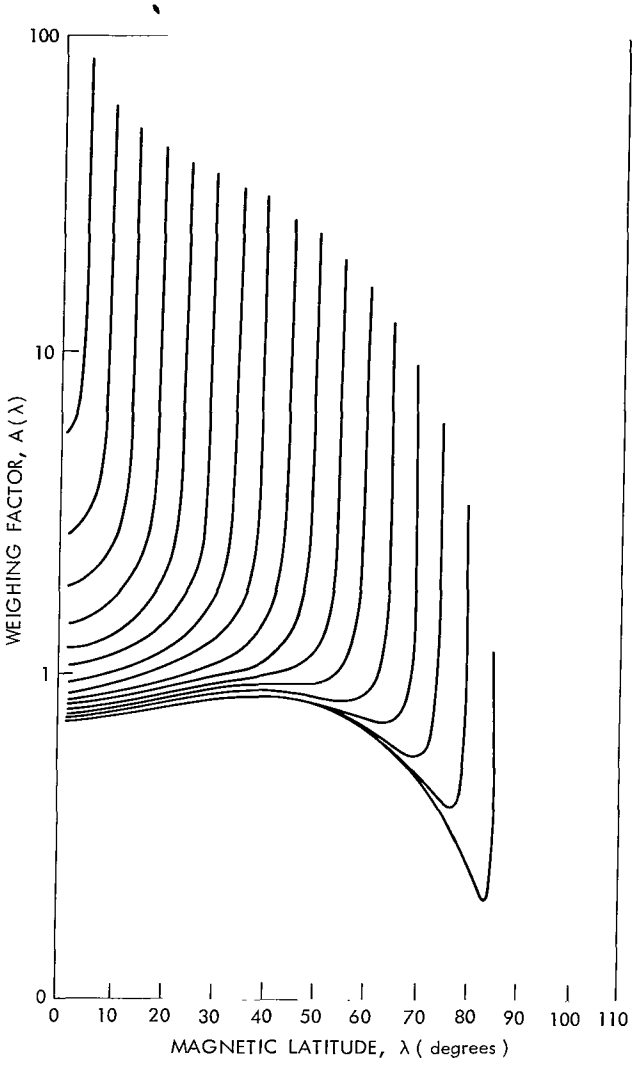

Figure 11—The weighing factor, A(λ), versus latitude for various mirror latitudes, λ_m, where the mirror latitudes (λ_m) are the asymptotes of each curve.

mirror point, than at latitudes less than 48°. To elaborate, if one assumes that the mirror latitude is very nearly equal to 90°, then from Equation 17

$$A(\lambda) \approx \frac{\cos\lambda\sqrt{4-3\cos^2\lambda}}{1.414} \quad .$$

To find the point of inflection of A(λ), the derivative with respect to λ is set to zero. Solving the resulting equation, it turns out that

$$\lambda_{inflect} \approx 48^\circ \quad .$$

Checking Figure 11, one sees that in this region the curve begins to dip. To find the time spent per unit path length consider

$$V_{\|} = \frac{ds}{dt}$$

where $V_{\|}$ is the component of the velocity along the field line. By comparing Equations 15 and 16, the time spent per unit path length in terms of the weighting factor is

$$\frac{d\lambda}{dt} = \frac{1}{A(\lambda)}\frac{ds}{dt} = \frac{v\cos\alpha}{A(\lambda)} \quad .$$

For particles mirroring at large latitudes, the length of path per unit time at the equator is

$$\Delta\lambda \approx v \quad .$$

Whereas at $\lambda > 48^\circ$ where the pitch angle is still very near zero, the time spent per path length is greater than v since $A(\lambda > 48^\circ)$ is less than one.

The integrals of Equation 16 are numerically evaluated on a digital computer using Simpson's technique. At mirror latitudes, λ_m, the expression $A(\lambda_m)$ is undefined. In order to overcome this difficulty, Equation 16 is numerically integrated to $\lambda_m - \epsilon$ where ϵ is made arbitrarily small such that the values of the integrals do not change appreciably.

The last step is to eliminate the model parameter, S, for time in the solar cycle. A current estimate of the present solar cycle is given by Figure 12. This has been constructed from information obtained from Harris and Priester (Reference 15). An extrapolation beyond 1961 has been

made to order to estimate the flux at the present time which is near solar minimum. The constructed mean solar cycle with epoch at January, 1954 is assumed to be 11 years duration. The unsymmetrical nature of the cycle will produce interesting effects on the proton population, as will be seen in the following discussion of the results.

RESULTS

Equation 11 is numerically integrated on a digital computer using a fourth-order Runge-Kutta technique with the initial conditions of $N(E) = 0$ and t = solar minimum. The termination criterion is that a given cycle proton density is the same as the preceding cycle proton density within an accuracy tolerance of less than 1%. Figure 13 is a plot of time to reach the termination criterion in terms of solar cycles (that is, 11 years) versus energy for a typical line of force, $L = 1.25$. As can be seen, the time required to build the steady-state condition is rather long for low values of field strength. A build-up time of 10 solar cycles corresponds roughly to 700 km in minimum altitude. Below a $B \approx 0.22$ gauss, which corresponds roughly to a minimum altitude of 250 km, the test for steady-state is difficult to detect due to the very low proton density and the almost constant atmospheric density.

Table 1 gives the figure numbers of the B-L points considered for this report. The first figure number refers to the plot of the proton flux time history while the second refers to the proton flux spectrum plot.

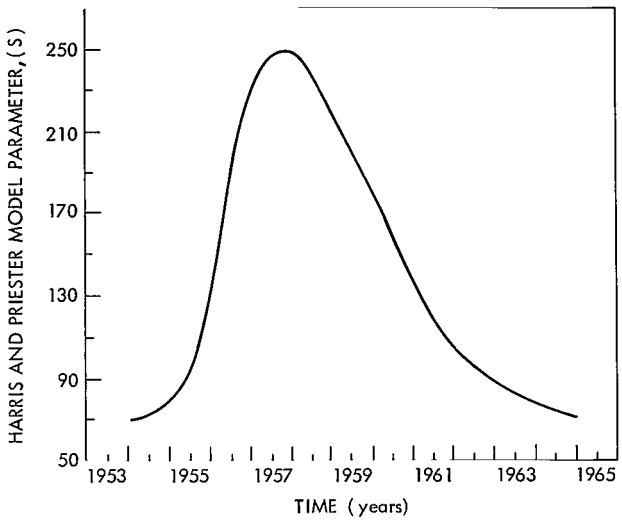

Figure 12—A time history of the constructed mean solar cycle variation of the Harris and Priester model parameter, S, with reference time t_0 of June, 1954.

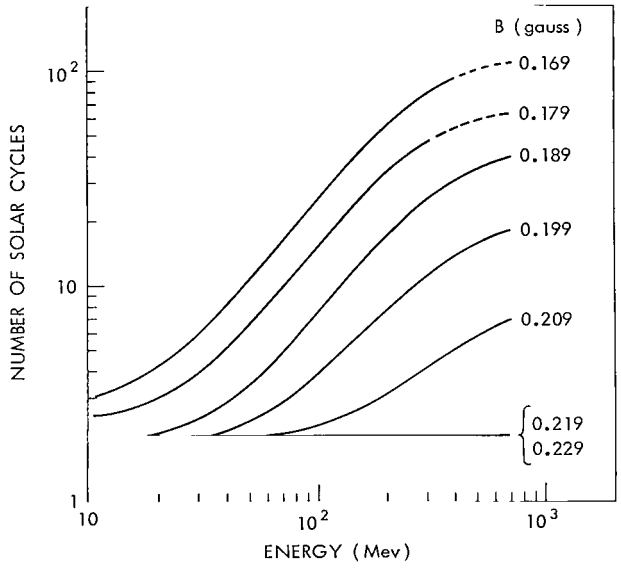

Figure 13—The time required in terms of solar cycles to build steady-state conditions versus energy as a function of B for $L = 1.25$ e.r.

Figures 14 through 40 are time histories of the proton flux for lines of force, ranging from $L = 1.188$ to 1.600 and various minimum altitudes, after the aforementioned steady-state condition has been satisfied. It is seen from these graphs that higher energy protons are not extremely affected by the solar-cycle variations, whereas the lower energy protons vary considerably with the cycle. Due to the "sluggishness" of the higher energy protons, the phase between proton flux

Table 1

Summary of B-L Points.

Figure Number		L (e.r.)	B (gauss)	λ (degs.)	h_{min} (kms.)
Time History	Energy Spectra				
14	41	1.1880	.1864	.954	710
15	42		.1884	2.954	650
16	43		.1930	4.954	580
17	44		.2075	8.954	400
18	45		.2189	10.954	290
19	46	1.2500	.1677	5.945	900
20	47		.1741	7.945	810
21	48		.1830	9.945	710
22	49		.1936	11.945	580
23	50		.2070	13.945	410
24	51		.2240	17.945	210
25	52	1.3419	.1674	13.933	900
26	53		.1809	15.933	790
27	54		.1974	17.933	550
28	55		.2173	19.933	350
29	56	1.4000	.1661	16.924	1050
30	57		.1821	18.924	860
31	58		.2014	20.924	600
32	59		.2250	22.924	330
33	60	1.5000	.1727	21.908	1050
34	61		.1936	23.908	750
35	62		.2190	25.908	450
36	63		.2501	27.908	130
37	64	1.6000	.1694	24.905	1100
38	65		.1926	26.905	800
39	66		.2208	28.905	480
40	67		.2557	30.905	150

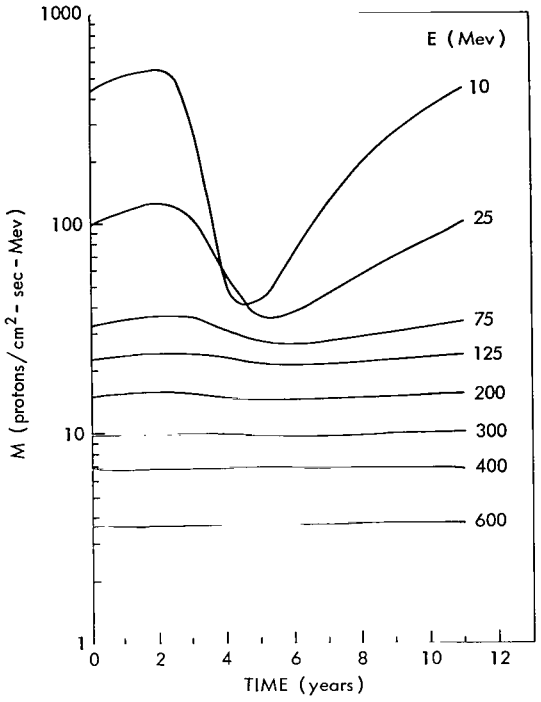

Figure 14—Proton time histories for L = 1.188, B = 0.1864, h_{min} = 710.

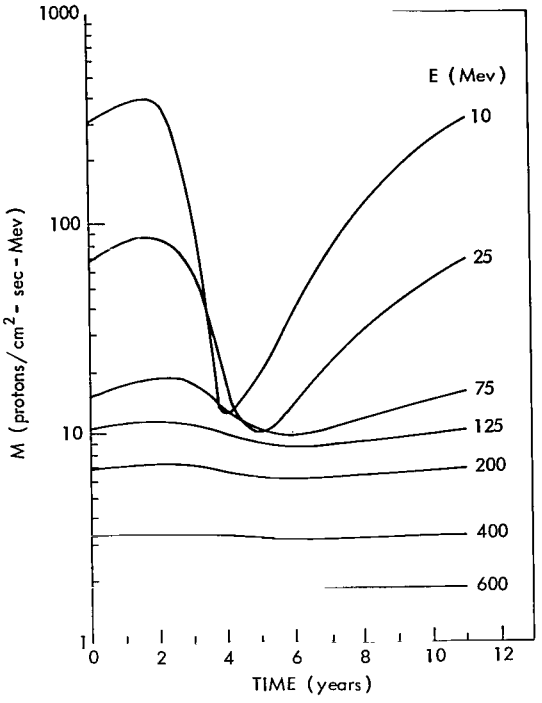

Figure 15—Proton time histories for L = 1.188, B = 0.1884, h_{min} = 650.

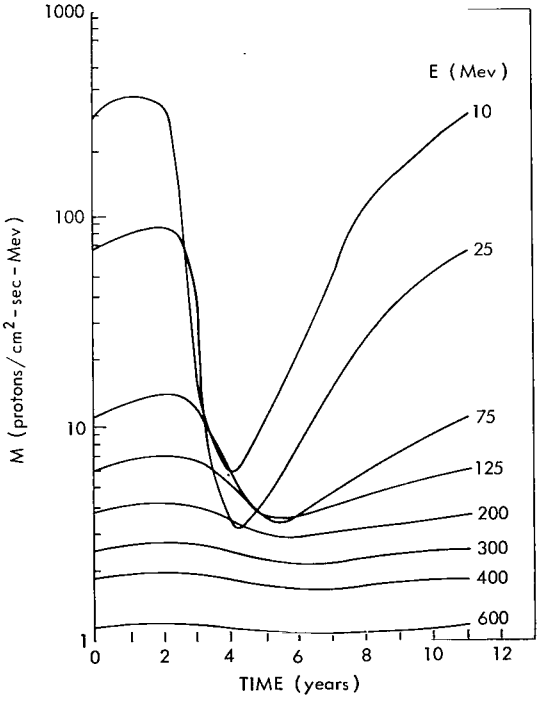

Figure 16—Proton time histories for L = 1.188, B = 0.193, h_{min} = 580.

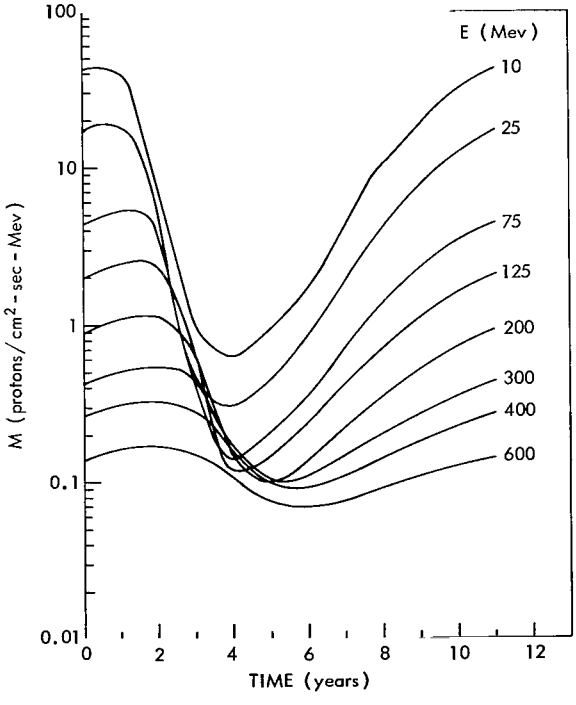

Figure 17—Proton time histories for L = 1.188, B = 0.2075, h_{min} = 400.

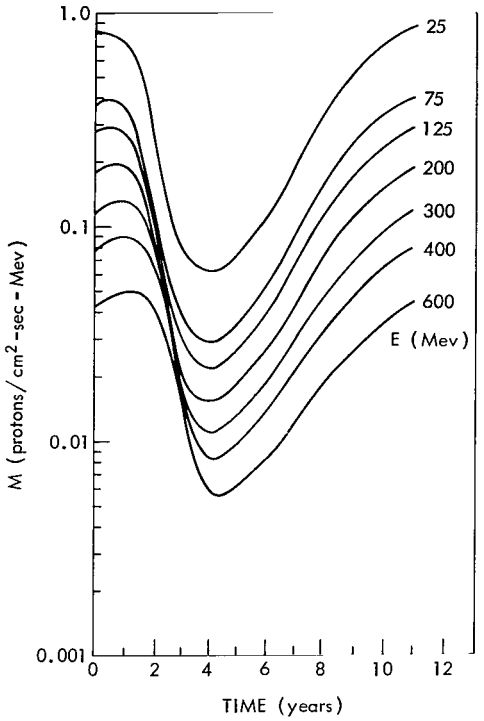

Figure 18—Proton time histories for L = 1.188, B = 0.2189, h_{min} = 290.

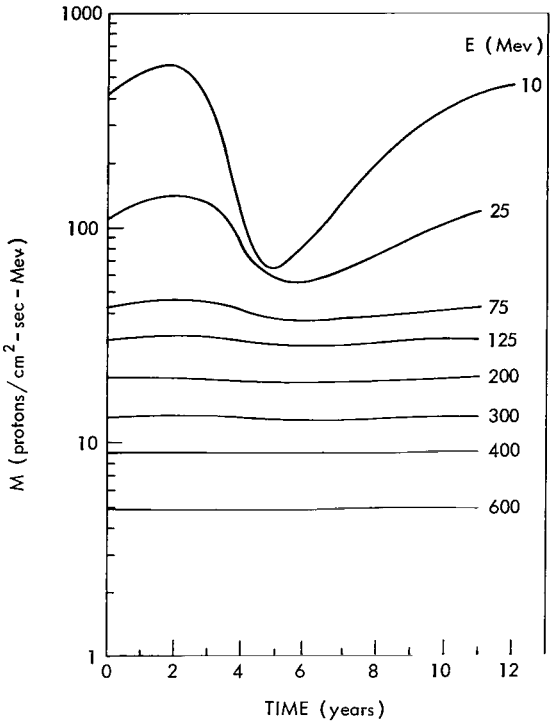

Figure 19—Proton time histories for L = 1.25, B = 0.168, h_{min} = 900.

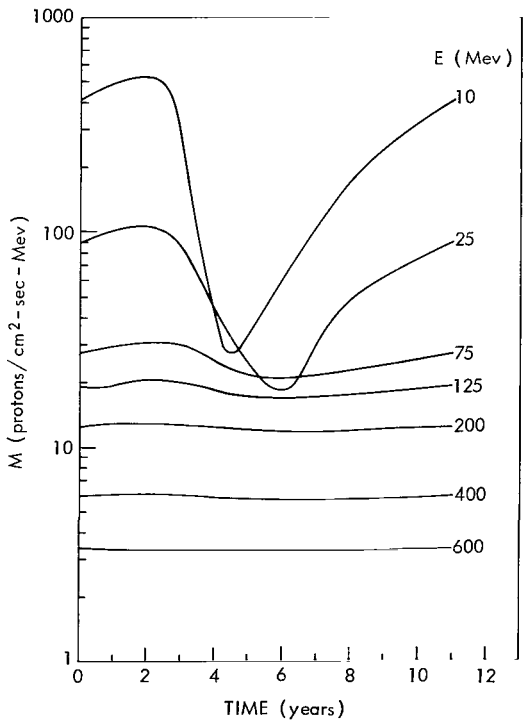

Figure 20—Proton time histories for L = 1.25, B = 0.1741, h_{min} = 810.

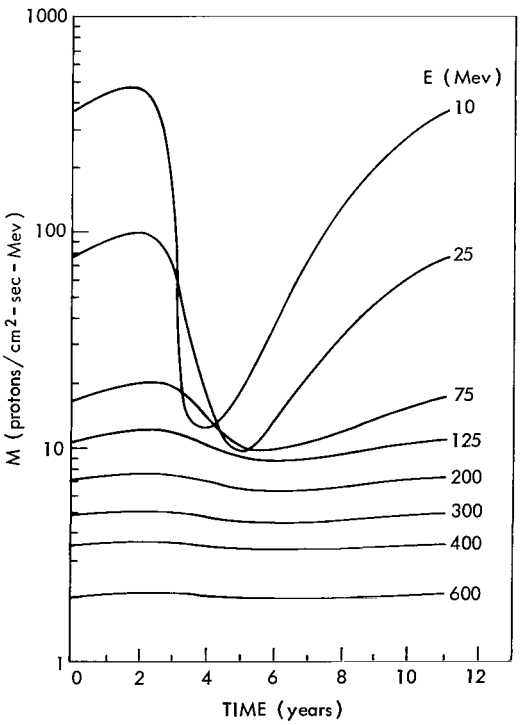

Figure 21—Proton time histories for L = 1.25, B = 0.183, h_{min} = 710.

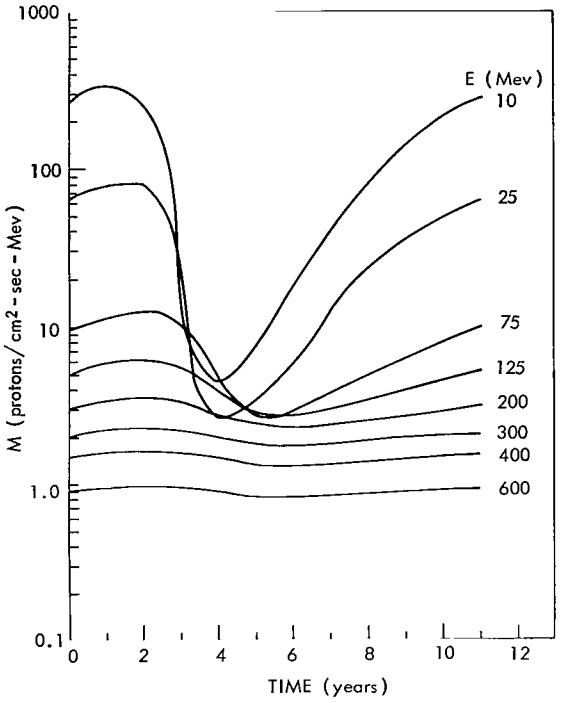

Figure 22—Proton time histories for L = 1.25, B = 0.194, h_{min} = 580.

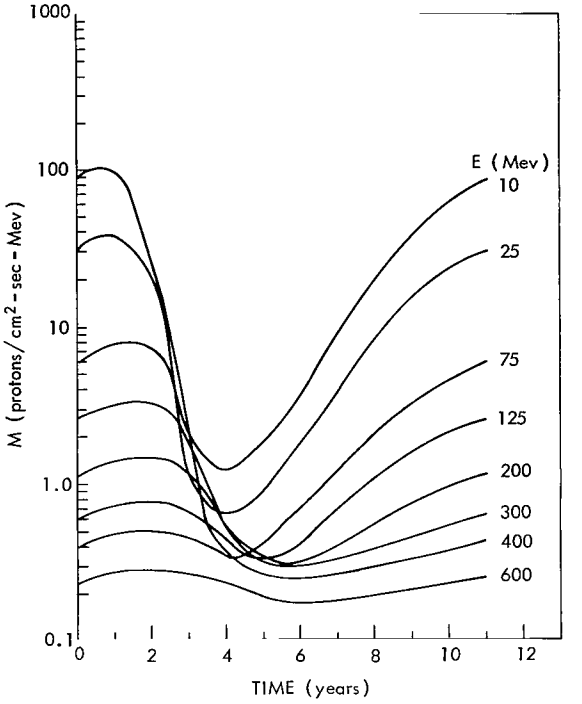

Figure 23—Proton time histories for L = 1.25, B = 0.207, h_{min} = 410.

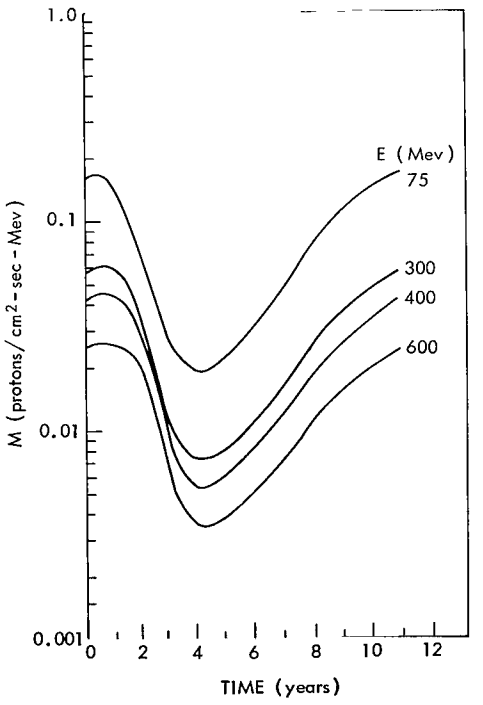

Figure 24—Proton time histories for L = 1.25, B = 0.2240, h_{min} = 210.

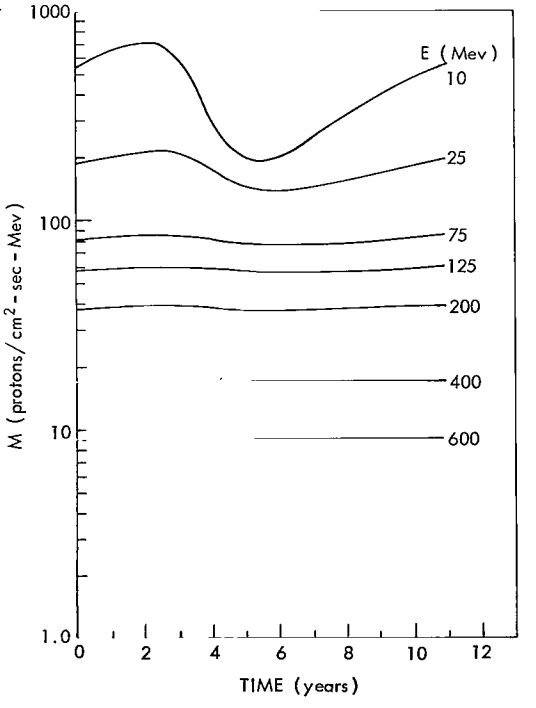

Figure 25—Proton time histories for L = 1.3419, B = 0.1674, h_{min} = 900.

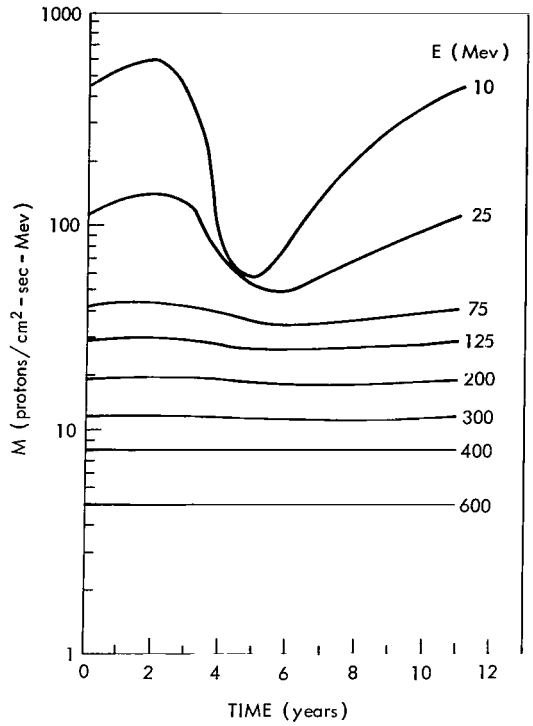

Figure 26—Proton time histories for L = 1.34, B = 0.181, h_{min} = 790.

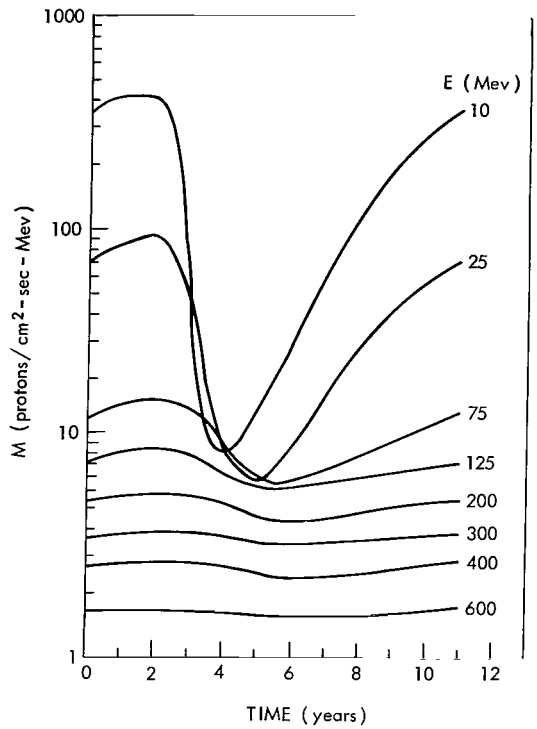

Figure 27—Proton time histories for L = 1.34, B = 0.197, h_{min} = 550.

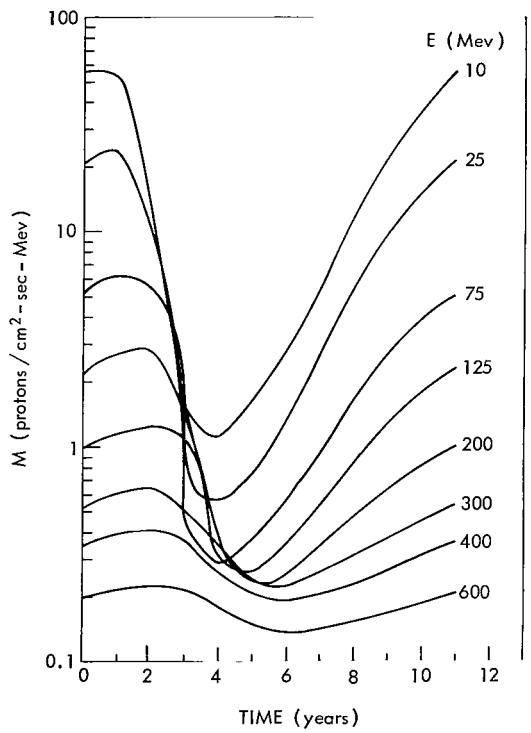

Figure 28—Proton time histories for L = 1.34, B = 0.217, h_{min} = 350.

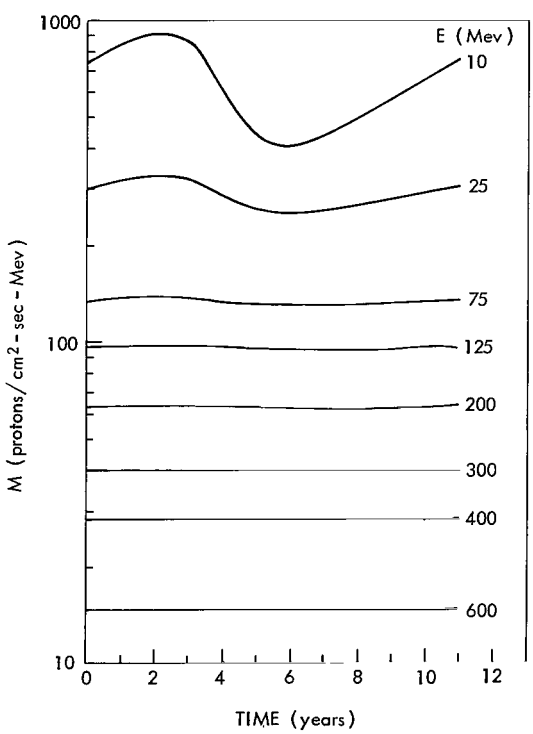

Figure 29—Proton time histories for L = 1.400, B = 0.1661, h_{min} = 1050.

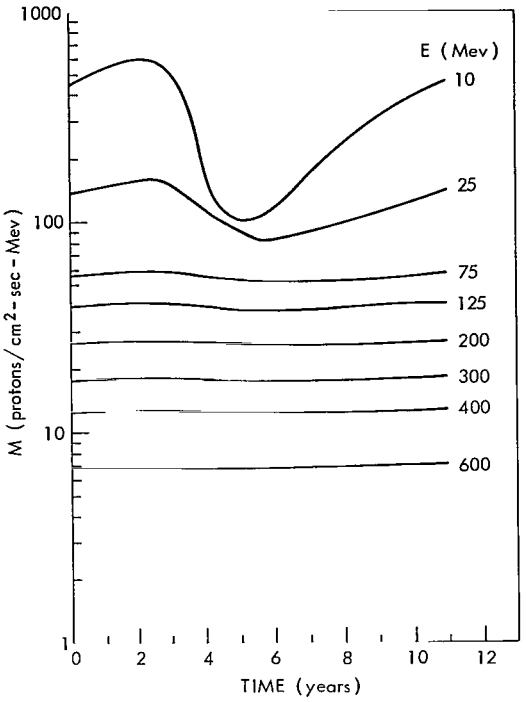

Figure 30—Proton time histories for L = 1.40, B = 0.1821, h_{min} = 860.

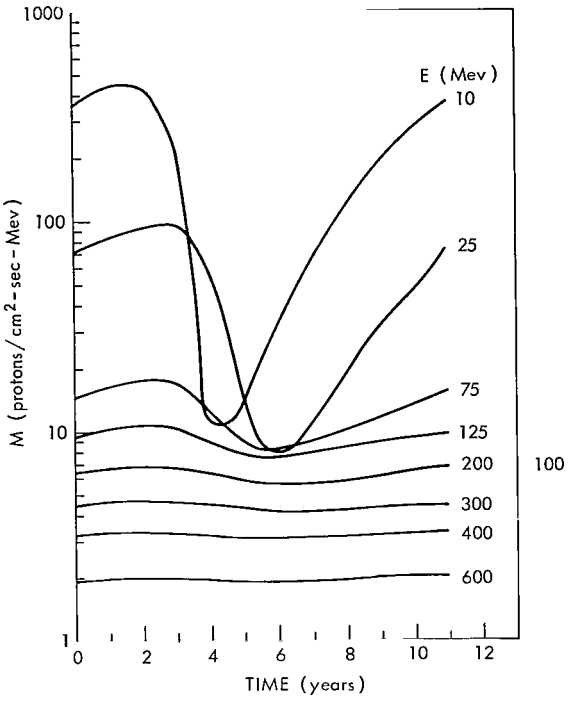

Figure 31—Proton time histories for L = 1.4, B = 0.2014, h_{min} = 600.

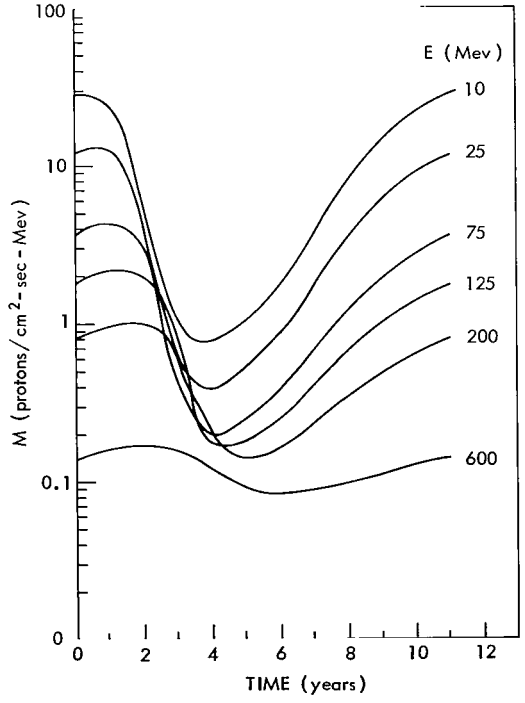

Figure 32—Proton time histories for L = 1.400, B = 0.225, h_{min} = 330.

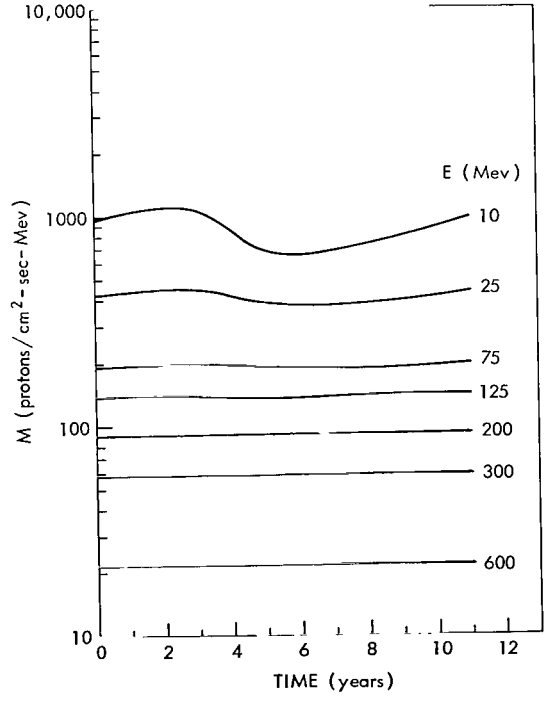

Figure 33—Proton time histories for L = 1.5, B = 0.1727, h_{min} = 1050.

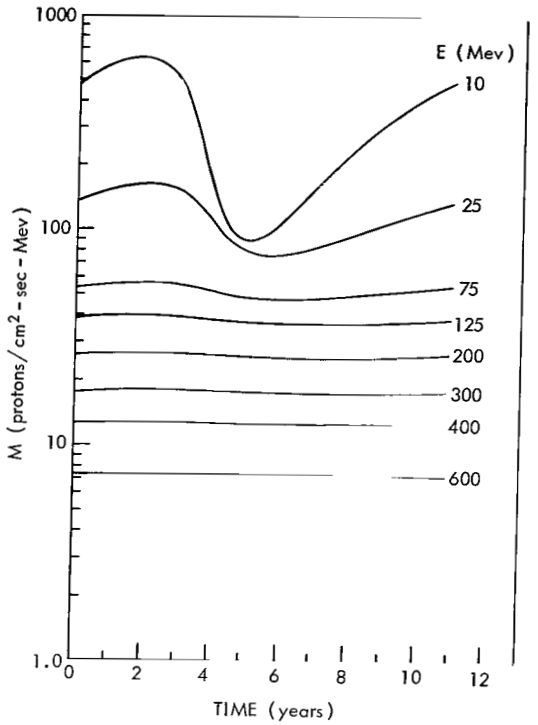

Figure 34—Proton time histories for L = 1.5, B = 0.1936, h_{min} = 750.

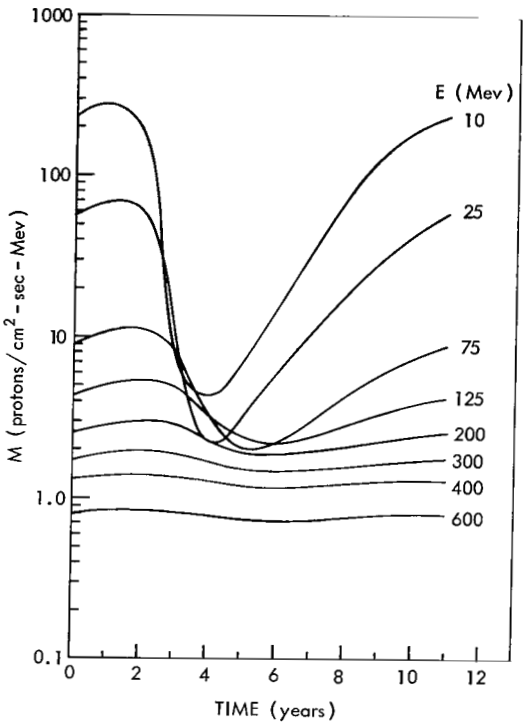

Figure 35—Proton time histories for L = 1.5, B = 0.2190, h_{min} = 450.

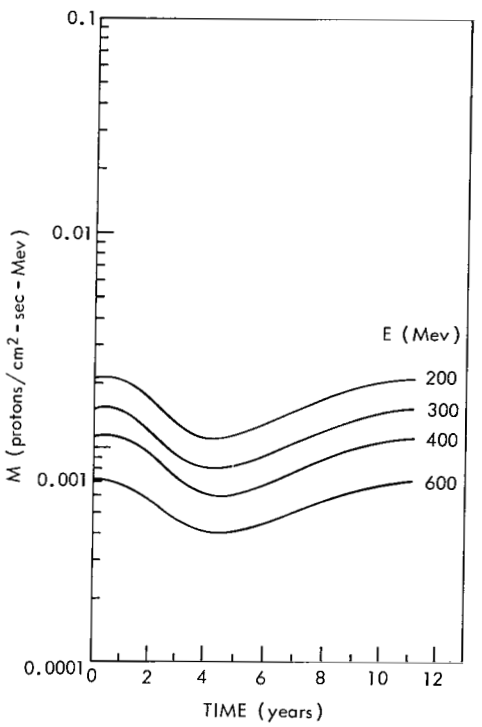

Figure 36—Proton time histories for L = 1.5, B = .2501, h_{min} = 130.

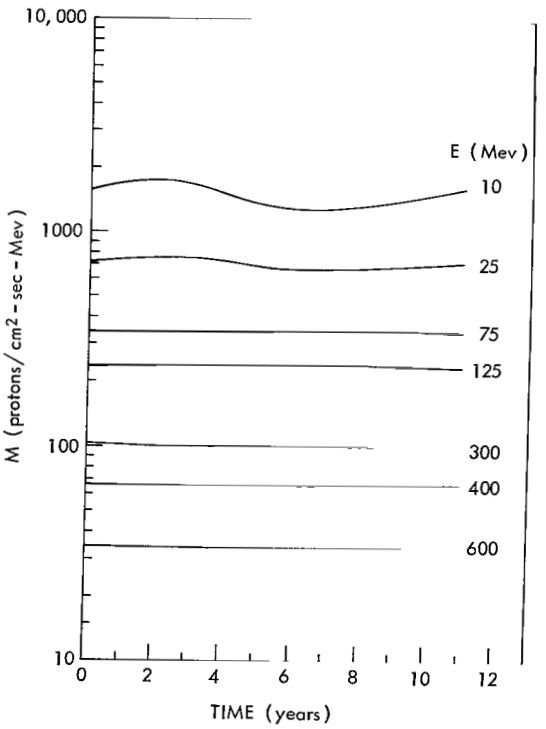

Figure 37—Proton time histories for L = 1.6, B = .1694, h_{min} = 1100.

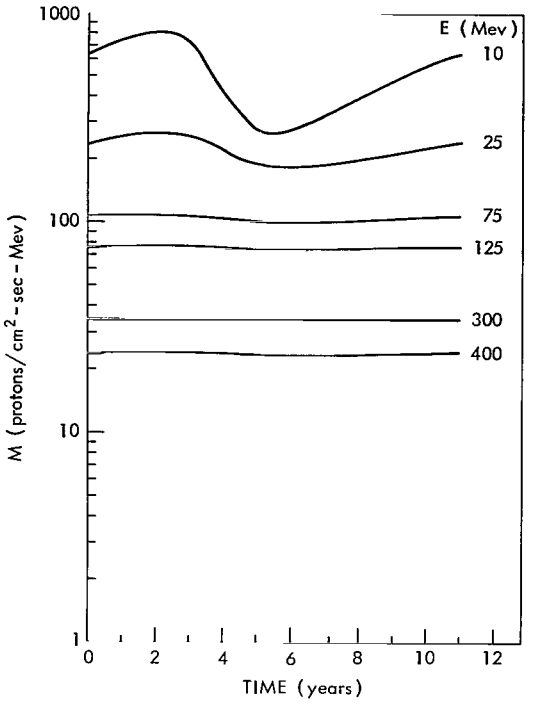

Figure 38—Proton time histories for L = 1.6, B = .1926, h_{min} = 800.

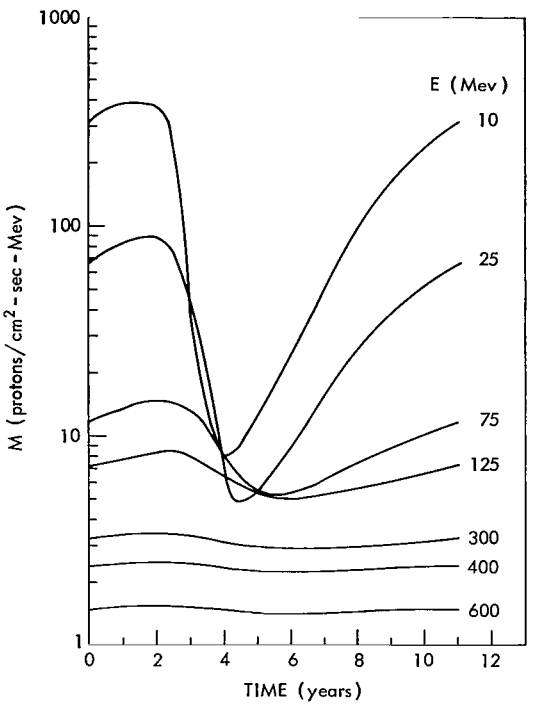

Figure 39—Proton time histories for L = 1.6, B = .2208, h_{min} = 480.

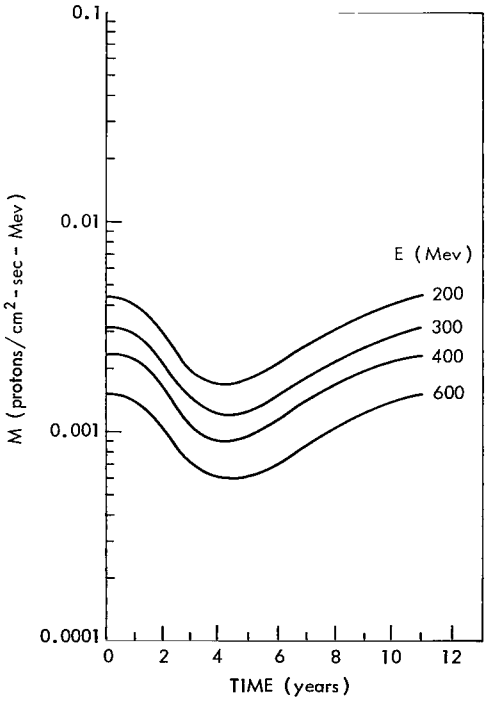

Figure 40—Proton time histories for L = 1.6, B = .2557, h_{min} = 150.

minimum and solar minimum (i.e., t = 4 years on the time scale) is shifted. As can be seen, the amount of shift depends on the proton's energy and position in space. In some instances this shifting of phase with respect to the solar cycle permits lower energy protons to be less abundant than higher energy protons, a result not readily apparent from the steady-state solution (that is, Equation 12).

Figures 41 through 67 are proton-flux energy spectra for different lines of force and various minimum altitudes at different times in the solar cycle. The dotted lines are the solution of Equation 12 at the two time extremes, solar minimum and solar maximum. The aforementioned solar-cycle effect of changing the nature of the energy spectrum is more apparent from these figures. It is interesting to note that as the minimum altitude for these curves approaches roughly 800 km, the solar cycle variation is almost negligible. It is evident now that a more efficient way to calculate the proton density in the upper region of space where h_{min} > 800 km is to average the number density over the solar cycle and apply the

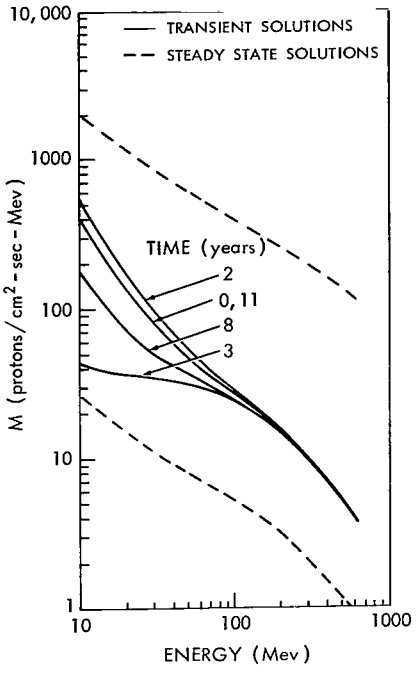

Figure 41—Proton energy spectra at different times in the solar cycle for L = 1.188, B = .1864, h_{min} = 710.

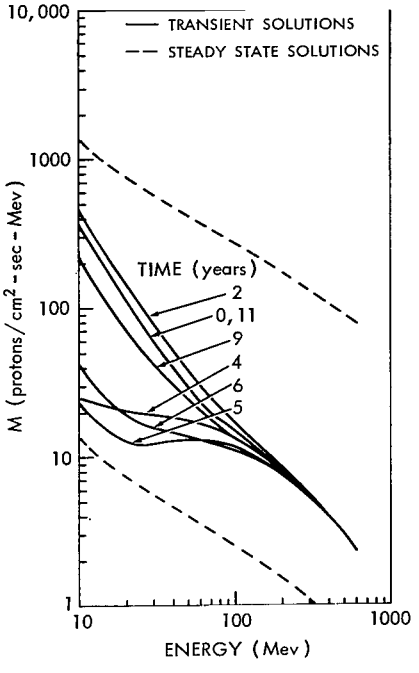

Figure 42—Proton energy spectra at different times in the solar cycle for L = 1.188, B = .1884, h_{min} = 650.

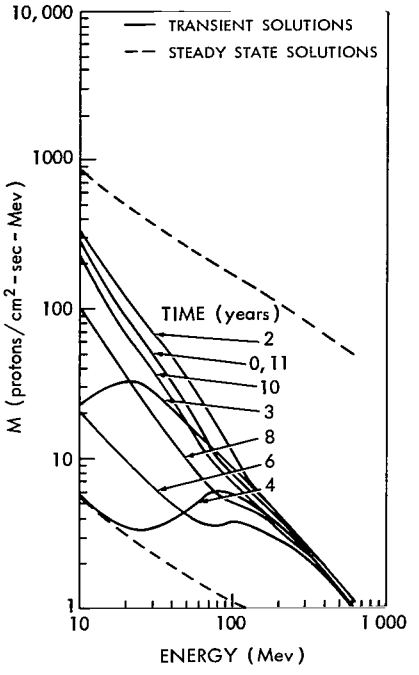

Figure 43—Proton energy spectra at different times in the solar cycle for L = 1.188, B = .193, h_{min} = 580.

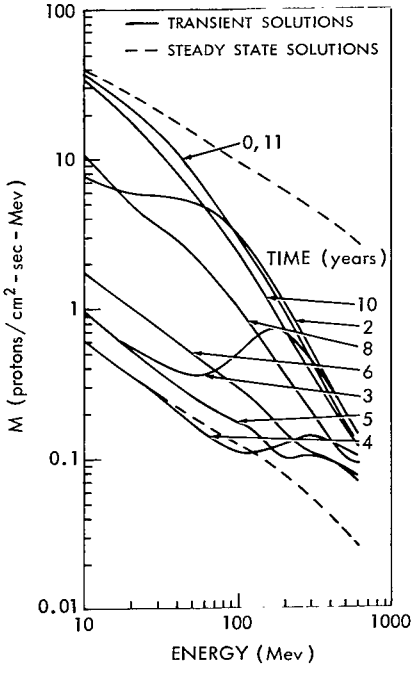

Figure 44—Proton energy spectra at different times in the solar cycle for L = 1.188, B = .2075, h_{min} = 400.

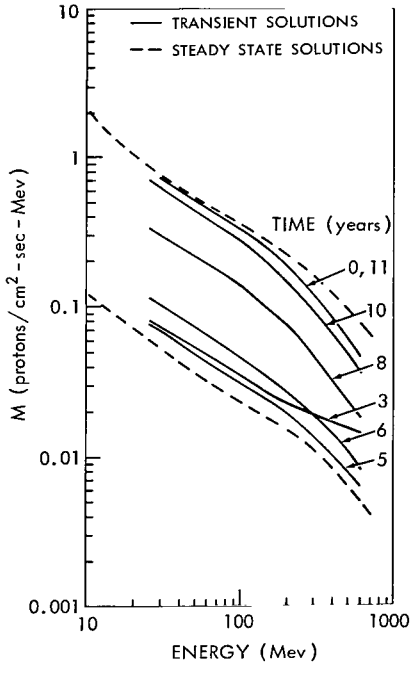

Figure 45—Proton energy spectra at different times in the solar cycle for L = 1.1880, B = 0.2189, h_{min} = 290.

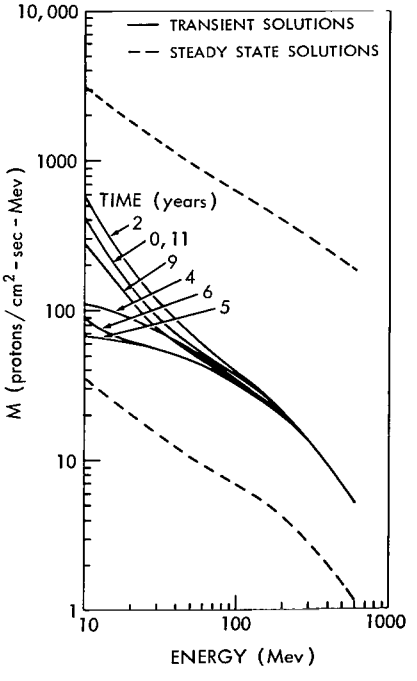

Figure 46—Proton energy spectra at different times in the solar cycle for L = 1.25, B = .1677, h_{min} = 900.

The curves are labeled by the time in years from solar minimum.

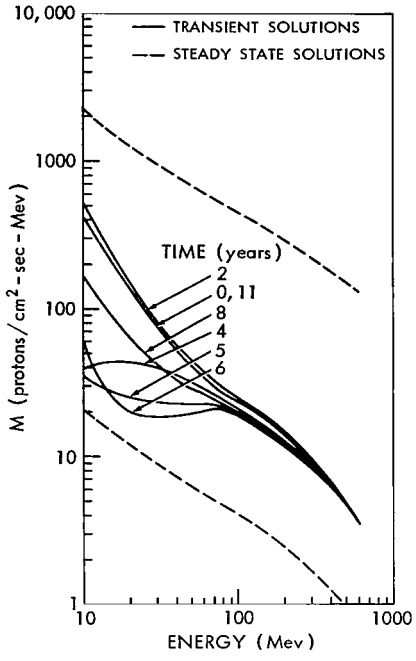

Figure 47—Proton energy spectra at different times in the solar cycle for L = 1.25, B = .1741, h_{min} = 810.

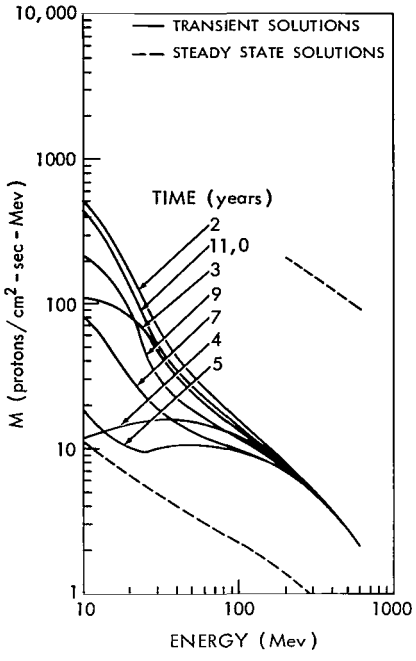

Figure 48—Proton energy spectra at different times in the solar cycle for L = 1.25, B = .183, h_{min} = 710.

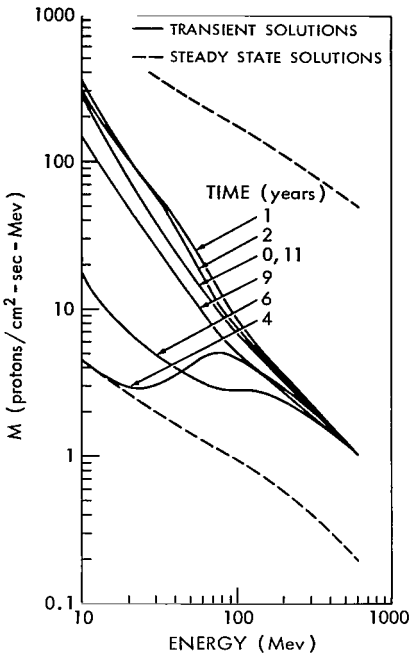

Figure 49—Proton energy spectra at different times in the solar cycle for L = 1.25, B = .1936, h_{min} = 580.

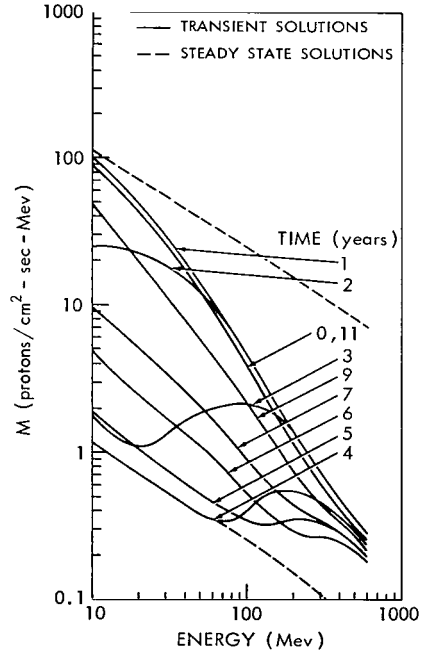

Figure 50—Proton energy spectra at different times in the solar cycle for L = 1.25, B = .207, h_{min} = 410.

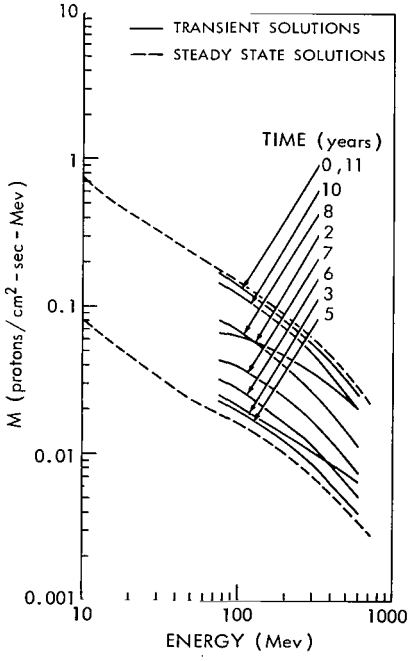

Figure 51—Proton energy spectra at different times in the solar cycle for L = 1.25, B = .2240, h_{min} = 210.

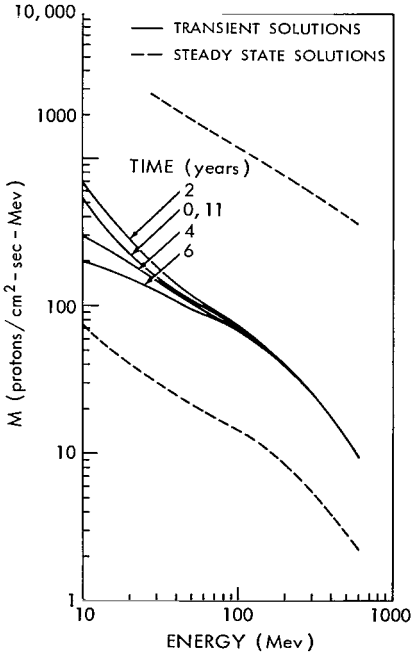

Figure 52—Proton energy spectra at different times in the solar cycle for L = 1.3419, B = .1674, h_{min} = 900.

The curves are labeled by the time in years from solar minimum.

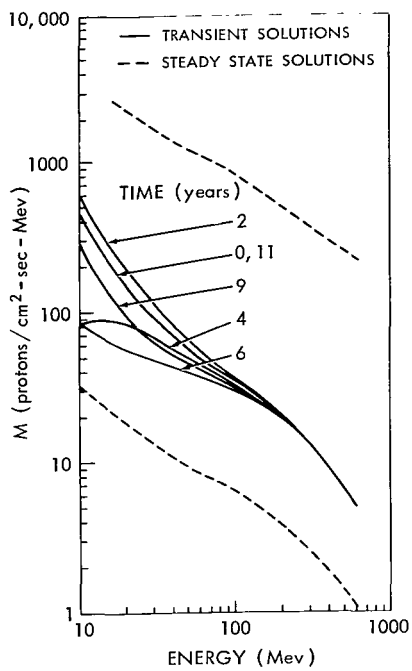

Figure 53—Proton energy spectra at different times in the solar cycle for L = 1.3419, B = .1809, h_{min} = 790.

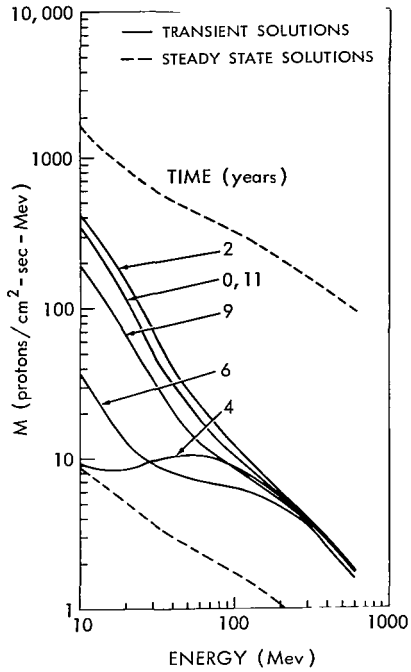

Figure 54—Proton energy spectra at different times in the solar cycle for L = 1.3419, B = .1974, h_{min} = 550.

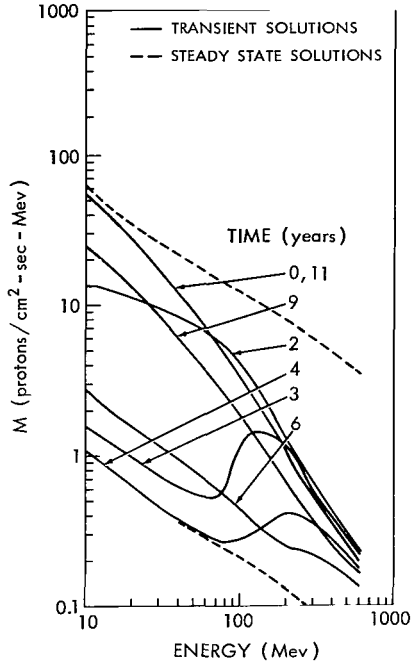

Figure 55—Proton energy spectra at different times in the solar cycle for L = 1.3419, B = .2173, h_{min} = 350.

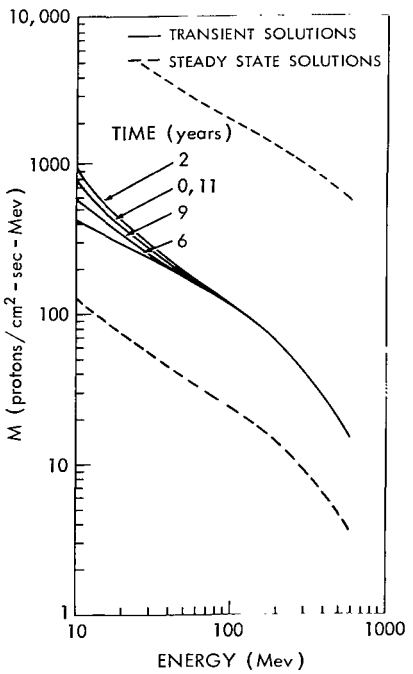

Figure 56—Proton energy spectra at different times in the solar cycle for L = 1.400, B = .1661, h_{min} = 1050.

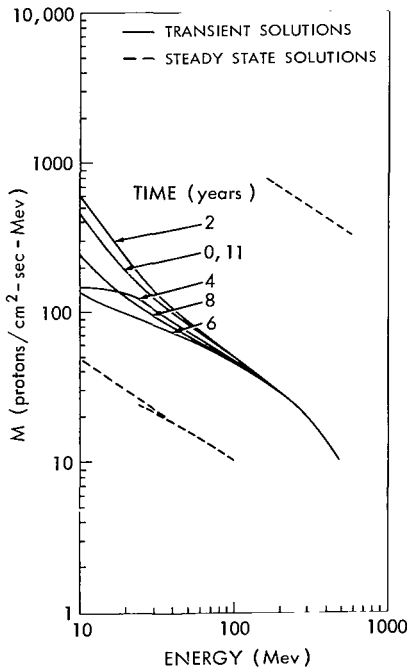

Figure 57—Proton energy spectra at different times in the solar cycle for L = 1.400, B = .182, h_{min} = 860.

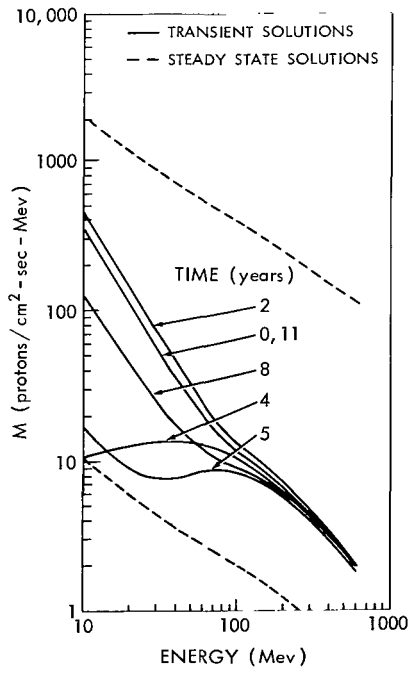

Figure 58—Proton energy spectra at different times in the solar cycle for L = 1.400, B = .2014, h_{min} = 600.

The curves are labeled by the time in years from solar minimum.

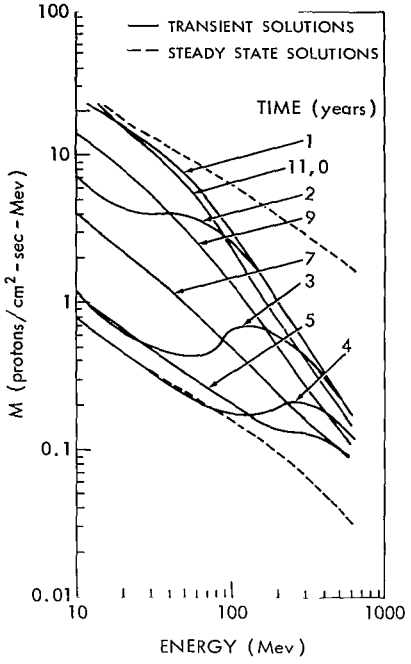

Figure 59—Proton energy spectra at different times in the solar cycle for L = 1.40, B = .225, h_{min} = 330.

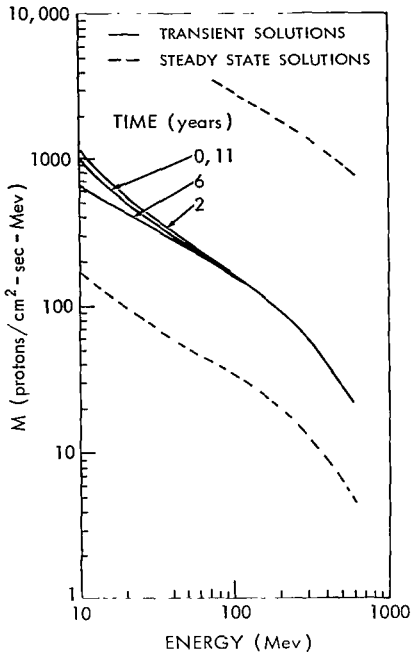

Figure 60—Proton energy spectra at different times in the solar cycle for L = 1.5, B = .1727, h_{min} = 1050.

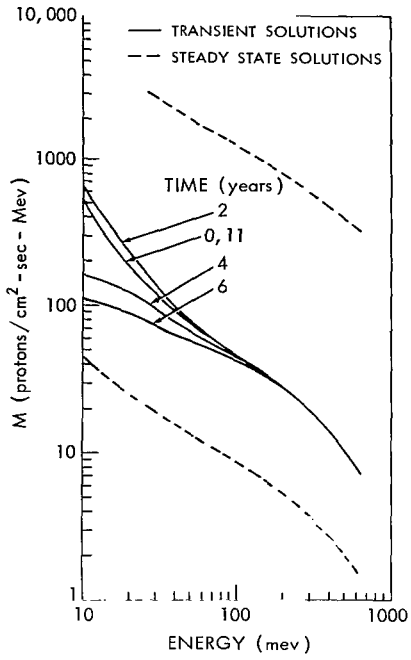

Figure 61—Proton energy spectra at different times in the solar cycle for L = 1.5, B = .1935, h_{min} = 750.

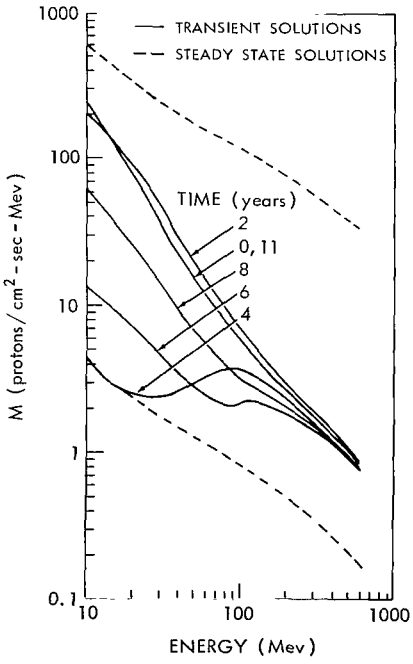

Figure 62—Proton energy spectra at different times in the solar cycle for L = 1.5, B = .2190, h_{min} = 450.

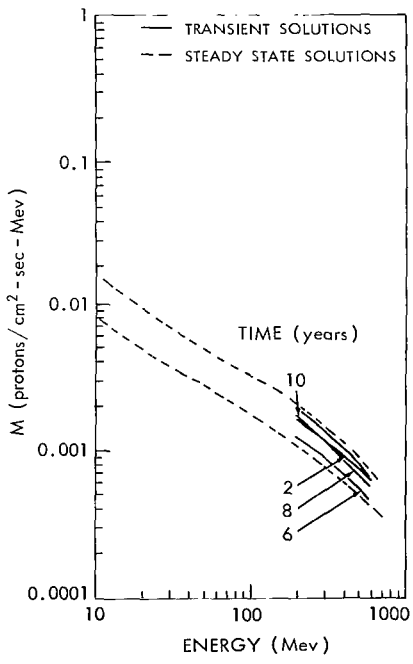

Figure 63—Proton energy spectra at different times in the solar cycle for L = 1.5, B = 0.2501, h_{min} = 130.

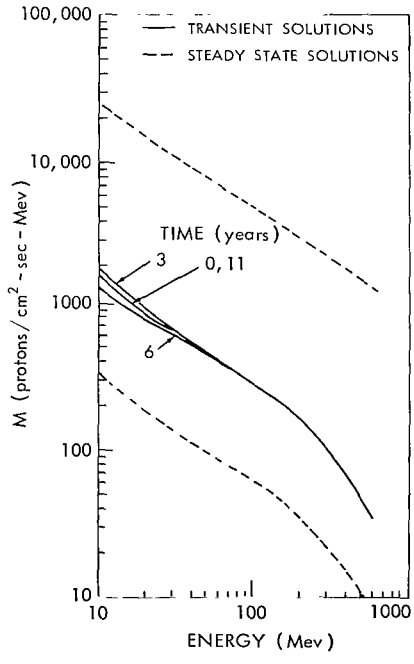

Figure 64—Proton energy spectra at different times in the solar cycle for L = 1.6, B = .1694, h_{min} = 1100.

The curves are labeled by the time in years from solar minimum.

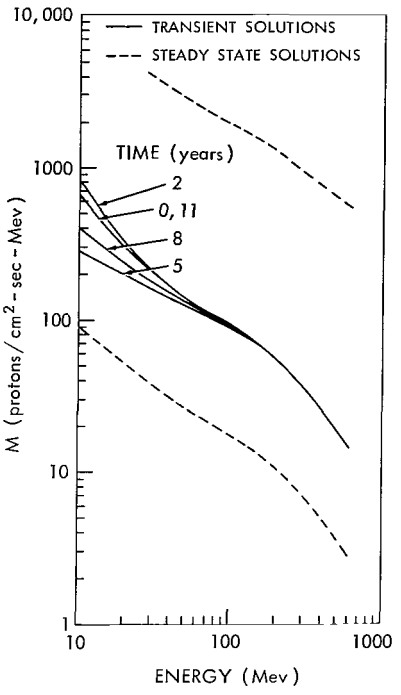

Figure 65—Proton energy spectra at different times in the solar cycle for L = 1.6, B = .1926, h_{min} = 800.

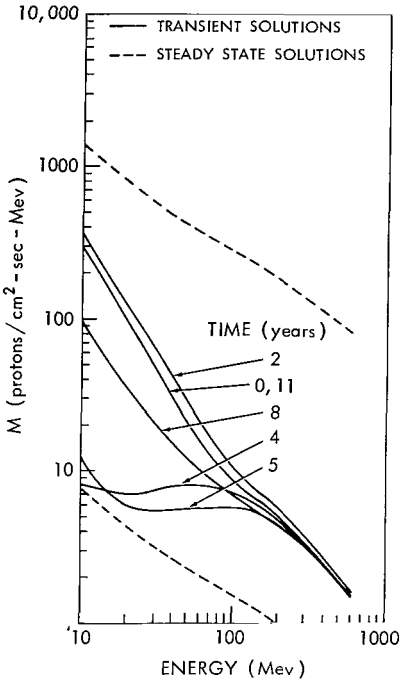

Figure 66—Proton energy spectra at different times in the solar cycle for L = 1.6, B = .2208, h_{min} = 480.

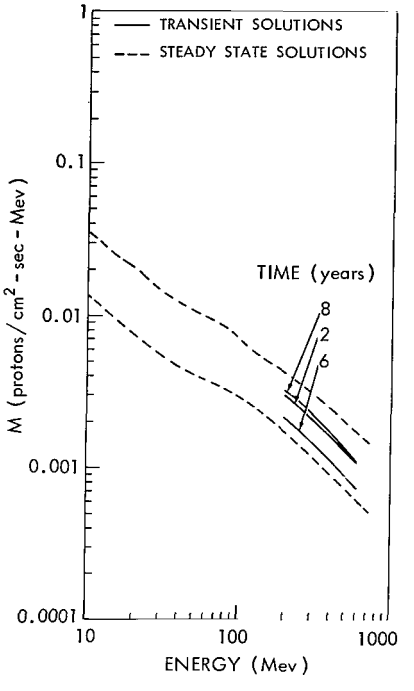

Figure 67—Proton energy spectra at different times in the solar cycle for L = 1.6, B = .2557, h_{min} = 150.

The curves are labeled by the time in years from solar minimum.

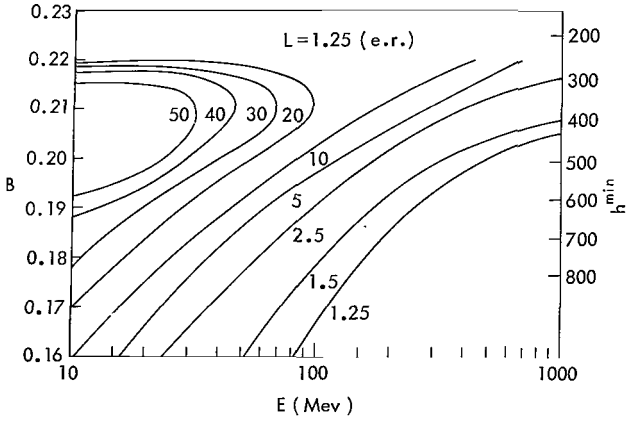

Figure 68—The amplitude of the proton population changes during the solar cycle for L = 1.25.

steady-state Equation 12 by averaging over the solar cycle. From Figure 13 it is apparent that this procedure would eliminate a great deal of numerical integration. A general procedure has been adopted to utilize this fact by calculating the ratio of proton flux at solar minimum to proton flux at solar maximum. Figures 68 and 69 are contours of this ratio plotted in B versus energy for various L lines. When the ratio, which depends on the proton's energy and position in space, is in the vicinity of one, the steady-state proton calculation with the solar-cycle averaged atmosphere will suffice.

It is seen from Figures 41 through 67 that the change in proton density from solar minimum to solar maximum is appreciable. The largest variations are found in the lower part of the energy spectrum. We may have overestimated the amplitude in this present calculation by as much as a factor of 2 because our solar cycle model uses S = 70 as a solar minimum while recent data of

Harris and Priester shows that S = 100 is probably more appropriate. Changing the shape of the mean solar cycle (Figure 12) will also affect the results of the calculation. It is expected that a more symmetrical cycle would affect the shape of the energy spectrums presented in Figures 41 through 67.

A comparison of past experimental results and the calculations of this paper is shown in Table 2. In discussing these experiments we can consider three types of information:

1. Data obtained from individual experiments which run long enough (a year or

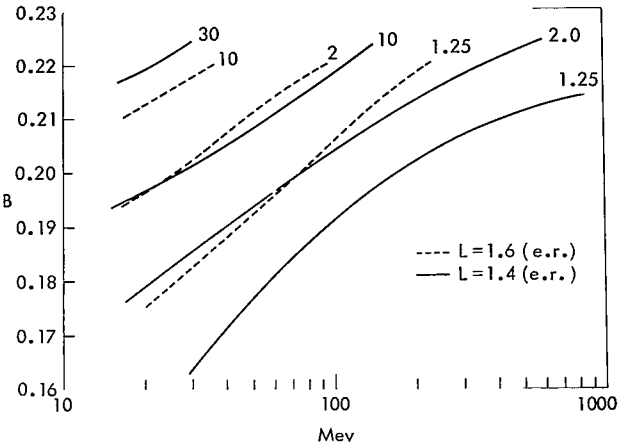

Figure 69—The amplitude of the proton population change during the solar cycle for L = 1.4 and 1.6.

Table 2

Comparison of Experimental Results of Inner Zone Proton Measurements with the Calculations in Present Paper.

Experiment	Date of Experiment	Time in Solar Angle	L	B	H Min.	Results of Experiment	Predictions from Present Paper
(a) Naugle and Kniffen (1963) — Emulsions on NERV	Sept. 1960	6.7	(a) 1.54	.209	610 km	Spectrum flat from 20 to 60 MeV J_0 (31) at 6.7 J_0 (31) at 4.1 (Exp. IV) $\overset{k}{\cdot}$	Spectrum should fall about a factor of 3 in this energy range (Fig. 28, curve 7) J_0 (31) at 6.7 J_0 (31) at 4 $\overset{}{\cdot}$ = 1.3 (Fig. 28)
			(b) 1.47	.223	400 km	Spectrum flat from 20 to 100 Mev J_0 (31) at 6.7 J_0 (31) at 4.1 (Exp. IV) $\overset{2.5}{\cdot}$	Spectrum should fall about a factor of 4 in this energy range (Fig. 27, curve 7) J_0 (31) at 6.7 J_0 (31) at 4 $\overset{}{\cdot}$ 3.5 (Fig. 27)
(b) Freden and White (1962) — Emulsions on Atlas	1960	6.5	1.40	.202	600 km	Spectrum peaks at 40 Mev J_0 (20) J_0 (40) 75	No spectral peak at t = 6.5 (Fig. 28) J_0 (20) J_0 (40) 2.0 but at t = 5 do have spectral peak $\frac{J_0\ (20)}{J_0\ (40)}$ = 0.9
(c) Pizzella, McIlwain and Van Allen — G M counter on Exp. VII	Oct. 1959 to Dec. 1960	5.8 to 7.0	1.40	.22	390 km	J_0 (E 18) at 7.0 J_0 (E 18) at 6.0 2.3	J_0 (E 25) at 7.0 J_0 (E = 25) at 6.0 = 2.0 (Fig. 24)
(d) Filz and Yagoda — Emulsions on Discoverer	Dec. 1960 to June 1962	7.0 to 8.5	varying	varying	400 km	J_0 (E 55) at 8.5 J_0 (E 55) at 7.0 2.0	J_0 (E = 75) at 8.5 J_0 (E = 75) at 7.0 2.3 (Fig. 24)
(e) Heckman and Nakano — Emulsions on Low altitude polar satellites	Sept. 1962 to Sept. 1963	8.7 to 9.7	varying	varying	400 km	J_0 (65) at 9.5 J_0 (65) at 9.0 = 1.0 ± 10 J_0 (65) at 9.5 J_0 (65) at 4.1 (Exp. IV) $\overset{3}{\cdot}$	J_0 (65) at 9.5 J_0 (65) at 9.0 = 1.2 J_0 (65) at 9.5 J_0 (65) at 4.1 = 12
(f) Freden and Paulikos — Solid state counters on Polar satellites	Sept. and Oct. 1962	8.8	1.30	.200	530 km	$\frac{J_0\ (7)}{J_0\ (85)}$ 13	
			1.47	.223	400 km	$\frac{J_0\ (7)}{J_0\ (85)}$ 23	$\frac{J_0\ (10)}{J_0\ (85)}$ 11 (Fig. 27)
			1.54	.209	610 km	$\frac{J_0\ (7)}{J_0\ (85)}$ 43	$\frac{J_0\ (10)}{J_0\ (85)}$ 24 (Fig. 28)
			low	high		J (E 31) at 8.8 J (E 31) at 4.1 (Exp. IV) $\overset{3}{\cdot}$	J (E = 50) at 8.8 J (E = 50) at 4.1 = 13
(g) Rowland Bakke, Imhof, Smith (1963) scintillators on Atlas pods	March 1963	9.2	1.27	.216	340 km	no maximum at 40 Mev $\frac{J_0\ (20)}{J_0\ (40)}$ 2.0 $\frac{J_0\ (10)}{J_0\ (60)}$ 8.0	$\frac{J_0\ (20)}{J_0\ (40)}$ = 2.2 (Fig. 26) $\frac{J_0\ (10)}{J_0\ (60)}$ = 9.0

more) so that they can see proton-flux changes directly. From Table 2, experiments (c) and (d) are of this type. Although experiment (d) is not one experiment on one satellite, it is many identical experiments on essentially identical satellites and therefore falls in this category.

2. Data on proton-flux changes obtained by comparing experiments on different satellites. Data of this type is given in experiments (a), (e) and (f) in Table 2.

3. Data given by direct measurement of the proton energy spectrum in one experiment. Experiments (a), (b), (e), (f) and (g) are of this type.

In comparing flux time change experiment of type 1 with the calculations, the agreement is good. Two experiments covering the period 1959 to 1962 give results consistent with the calculations.

Comparing with type 2 data does not work as well. The observed changes of flux with time agree qualitatively with those predicted, but not quantitatively. The experimental flux ratios are smaller than the calculated ones. Two remarks are in order here: First, type 2 data usually has larger errors attached to it than type 1 because it involves the systematic errors of two experiments while type 1 data involves no systematic errors (only statistical errors are involved in the time variations in the flux). Because of this the experimental flux ratios using type 2 data are probably not as accurate as those using type 1 data. Secondly, all the comparisons of type 2 data involve Explorer IV data, so there is no independent check of experimental consistency.

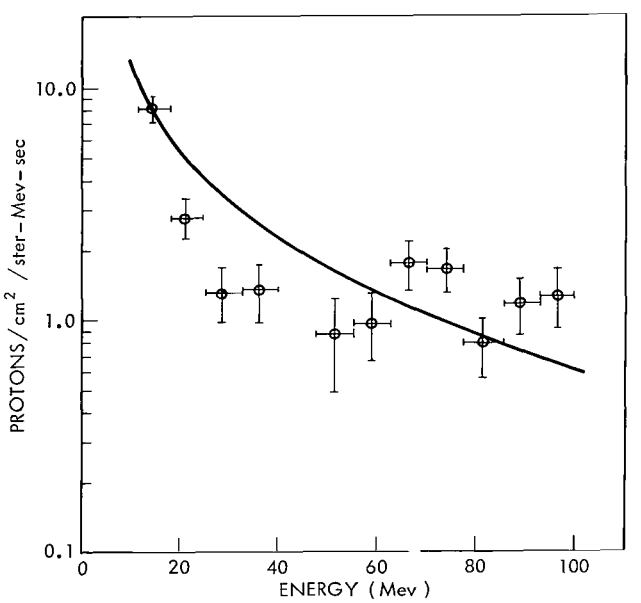

Figure 70—The energy spectrum of inner zone protons measured by Rowland et al, 1963 on an Atlas pad at L = 1.27, B = .216.

Shown for comparison is the spectrum calculated in this paper for L = 1.27, B = .207, $t \simeq 9$.

Of the five experiments of type 3 that help to understand the proton energy spectrum, the first two ((a) and (b) in 1960) showed a modest sized peak at about E = 40 Mev. The more recent experiment (g) of Rowland et al (Reference 24) shown in Figure 70 does not show such a peak. The solid curve on Figure 70 represents the normalized results of the present calculations compared with the data of Rowland. The agreement is fairly good. Recent experiments ((f) and (g)) show a large low-energy proton population but cannot be compared with early experiments because the early ones did not go down to such low energies. Figures 41 through 67 show that the calculated spectral shape should not change much during the period of these measurements, from 6 to 9 years solar-cycle time. The proton fluxes should increase but the shape of the spectrum stays nearly the same. Striking changes in spectral shape should occur on the

upswing of the solar cycle. The agreement with spectral shape in Figure 70 is not bad but the peaks in experiments (a) and (b) should not occur at t = 6. It may be that a neutron absorption as suggested by Freden and White (Reference 3) is required to explain the peak.

All of the data presented so far are mirror point fluxes, M, (i.e., the flux of protons mirroring per unit volume at one particular B and L). For low altitudes where the atmosphere changes rapidly with altitude, it is nearly correct to compare this flux with measured omnidirectional flux values, since, for these low altitudes, the omnidirectional flux is very nearly the same as the mirror-point flux. To show a more complete picture of the solar-cycle proton changes we have converted to omnidirectional fluxes using Equations 24 of Hess and Killeen (Reference 27). Figure 71 shows a calculated R - λ map of the 25 Mev proton omnidirectional fluxes, J, at solar maximum and solar minimum. An isoflux contour is clearly at lower R for solar minimum.

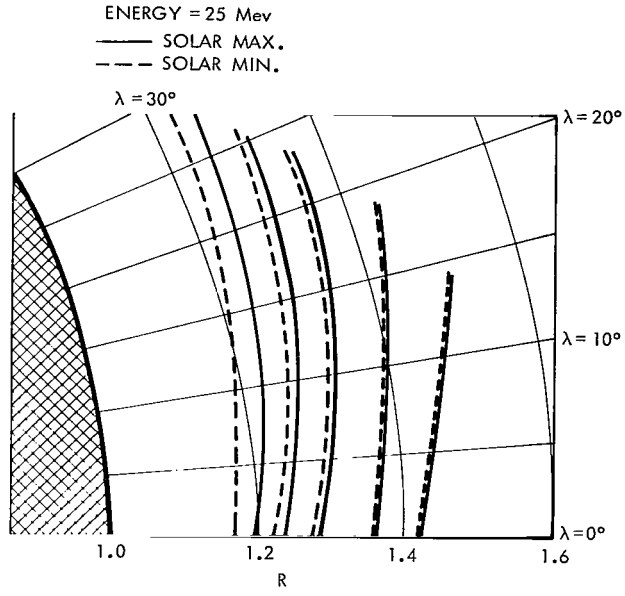

Figure 71—An R - λ map of the omnidirectional flux of E = 25 Mev protons at solar max and solar min.

CONCLUSIONS

In conclusion, large changes in proton fluxes will take place during the solar cycle for those regions of B-L space corresponding roughly to minimum altitudes of about 300-800 km. Changes in proton spectra will occur also. Comparison of the calculations with available experimental information are not conclusive. Some kinds of experimental data agree quantitatively with the calculations. Other data agrees qualitatively but not quantitatively. The crucial tests of the calculations will involve measuring changes in the proton flux and spectrum as we approach solar maximum during 1966-68. We know experimentally (Reference 16) that the atmospheric density changes used in the calculation are reasonable. These calculated effects must take place with about the magnitudes shown here unless there are features of the inner-belt protons which we do not now understand.

(Manuscript received June 4, 1965)

REFERENCES

1. Freden, S. C., and White, R. S., "Protons in the Earth's Magnetic Field," *Phys. Rev. Letters*, 3(1):9-11, July 1, 1959.

2. Freden, S. C., and White, R. S., "Particle Fluxes in the Inner Radiation Belt," *J. Geophys. Res.* 65(5):1377-1383, May 1960.

3. Freden, S. C., and White, R. S., "Trapped Proton and Cosmic Ray Albedo Neutron Fluxes," *J. Geophys. Res.* 67(1):25-29, January 1962.

4. Armstrong, A. H., Harrison, F. B., Heckman, H. H., and Rosen, L., "Charged Particles in the Inner Van Allen Radiation Belt," *J. Geophys. Res.* 66(2):351-357, February 1961.

5. Yoshida, S., Ludwig, G. H., and Van Allen, J. A., "Distribution of Trapped Radiation in the Geomagnetic Field," *J. Geophys. Res.* 65(3):807-813, March 1960.

6. McIlwain, C. E., "Coordinates for Mapping the Distribution of Magnetically Trapped Particles," *J. Geophys. Res.* 66(11):3681-3691, November 1961.

7. Pizzella, G., McIlwain, C. E., and Van Allen, J. A., "Time Variations of Intensity in the Earth's Inner Radiation Zone, October 1959 through December 1960," *J. Geophys. Res.* 67(4):1235-1253, April 1962.

8. Hess, W. N., "Discussion of Paper by Pizzella, McIlwain, and Van Allen 'Time Variations of Intensity in the Earth's Inner Radiation Zone. October 1959 through December 1960'," *J. Geophys. Res.* 67(12):4886-4887, November 1962.

9. Hess, W. N., "Lifetime and Time Histories of Trapped Radiation Belt Particles," GSFC Document X-640-63-96, May 1963.

10. Singer, S. F., "Trapped Albedo Theory of the Radiation Belt," *Phys. Rev. Letters,* 1(5):181-183, September 1, 1958.

11. Hess, W. N., "Van Allen Belt Protons from Cosmic-Ray Neutron Leakage," *Phys. Rev. Letters,* 3(1):11-13, July 1, 1959.

12. McDonald, F. B., and Webber, W. R., "A Study of the Rigidity and Charge Dependence of Primary Cosmic Ray Temporal Variations," *J. Phys. Soc. Japan,* 17(Suppl. A II):428-435, January 1962.

13. Aron, W. A., Hoffman, B. G., and Williams, R. C., *Range-Energy Curves,* 2d rev. 1949, Berkeley, Calif.: University of California Radiation Laboratory, AECU-663; UCRL-121, May 28, 1951.

14. Hess, W. N., "Energetic Particles in the Inner Van Allen Belt," *Space Sci. Ref.* 1(2):278-312, October 1962.

15. Harris, I., and Priester, W., "Time-Dependent Structure of the Upper Atmosphere," *J. Atmos. Sci.* 19(4):286-301, July 1962.

16. King-Hele, D. G., "Decrease in Upper-Atmosphere Density Since the Sunspot Maximum of 1957-1958," *Nature,* 198:832-834, June 1, 1963.

17. Bryant, R., "Densities Obtained from Drag on the Explorer XVII Satellite," *J. Geophys. Res.* 69(7):1423-1425, April 1964.

18. Spencer, N. W., Brace, L. H., Carignan, C. R., Taeusch, D. R., and Niemann, H., "The Concentration and Temperature of Molecular Nitrogen and Electrons in the 120- to 350-km Region," *Am. Geophys. Union Trans.* 44(4):884, December 1963 (Abstract).

19. Brace, L. H., and Spencer, N. W., "Geophysical Implications of Explorer 17 Electrostatic Probe Measurements," *Am. Geophys. Union Trans.* 44(4):884, December 1963 (Abstract).

20. Horowitz, R., and Newton, G. P., "First Direct In Situ Measurements of Atmospheric Density from Explorer 17 (1963 Iota)," *Am. Geophys. Union Trans.* 44(4):884, December 1963 (Abstract).

21. Reber, C. C., "Preliminary Results Regarding Neutral Atmosphere Composition from the Explorer 17 Satellite," *Am. Geophys. Union Trans.* 44(4):884, December 1963 (Abstract).

22. Hess, W. N., R. C. Blanchard, E. G. Stassinopoulos, "Average Solar Cycle Upper Atmosphere Densities in B-L Space," to be published in *Goddard Space Flight Center Contributions to COSPAR, May 1965,* NASA Technical Note D-3091.

23. Ray, C. E., "On the Theory of Protons Trapped in the Earth's Magnetic Field," *J. Geophys. Res.* 65(9):1125-1134, April 1960.

24. Rowland, J. H., Bakke, J. C., Imhof, W. L., and Smith, R. V., *Radiation Environment Experiment,* Palo Alto, Calif." Lockheed Missiles and Space Co., SSD-TDR-53-149; AD-413 129, June 1963.

25. Hess, W. N., and Killeen, J., "Spatial Distribution of Electrons from Neutron Decay in the Outer Radiation Belt," *J. Geophys. Res.* 66(11):3671-3680, November 1961.

3/18/85

"The aeronautical and space activities of the United States shall be conducted so as to contribute . . . to the expansion of human knowledge of phenomena in the atmosphere and space. The Administration shall provide for the widest practicable and appropriate dissemination of information concerning its activities and the results thereof."

—NATIONAL AERONAUTICS AND SPACE ACT OF 1958

NASA SCIENTIFIC AND TECHNICAL PUBLICATIONS

TECHNICAL REPORTS: Scientific and technical information considered important, complete, and a lasting contribution to existing knowledge.

TECHNICAL NOTES: Information less broad in scope but nevertheless of importance as a contribution to existing knowledge.

TECHNICAL MEMORANDUMS: Information receiving limited distribution because of preliminary data, security classification, or other reasons.

CONTRACTOR REPORTS: Technical information generated in connection with a NASA contract or grant and released under NASA auspices.

TECHNICAL TRANSLATIONS: Information published in a foreign language considered to merit NASA distribution in English.

TECHNICAL REPRINTS: Information derived from NASA activities and initially published in the form of journal articles.

SPECIAL PUBLICATIONS: Information derived from or of value to NASA activities but not necessarily reporting the results of individual NASA-programmed scientific efforts. Publications include conference proceedings, monographs, data compilations, handbooks, sourcebooks, and special bibliographies.

Details on the availability of these publications may be obtained from:

SCIENTIFIC AND TECHNICAL INFORMATION DIVISION

NATIONAL AERONAUTICS AND SPACE ADMINISTRATION

Washington, D.C. 20546